Epitaxial growth and surface properties of half-metal NiMnSb films

Epitaxial growth and surface properties of half-metal NiMnSb films

C N Borca[1], **D Ristoiu**[2], **H-K Jeong**[3], **Takashi Komesu**[4], **A N Caruso**[5], **J Pierre**[2], **L Ranno**[2], **J P Nozières**[2] and **P A Dowben**[4]

[1] Swiss Light Source and the Laboratory for Waste Management, Paul Scherrer Institute, Viligen PSI CH-5232, Switzerland
[2] Laboratoire Louis Néel, CNRS, BP166X, 38042 Grenoble Cedex, France
[3] Department of Physics, SungkyunKwan University, Jangan Suwon 440-746, Korea
[4] Department of Physics and Astronomy and the Center for Materials Research and Analysis, Behlen Laboratory of Physics, University of Nebraska, Lincoln, NE 68588-0111, USA
[5] Center for Nanoscale Science and Engineering, North Dakota State University, Fargo, ND 58047, USA

E-mail: camelia.borca@psi.ch

Abstract

We present, herein, an extended study of the half-Heusler alloy NiMnSb, starting with the deposition technique, continuing with the basic structural and magnetic properties of the thin films, and finishing with the electronic and compositional properties of their surfaces. The experimental methods we apply combine magnetization and magnetoresistivity measurements, atomic force microscopy, ferromagnetic resonance, x-ray and neutron diffraction, low energy electron diffraction, angle resolved x-ray photoemission, extended x-ray absorption fine structure spectroscopy, soft x-ray magnetic circular dichroism and spin polarized inverse photoemission spectroscopy. We find that stoichiometric surfaces exhibit close to 100% spin polarization at the centre of the surface Brillouin zone at the Fermi edge at ambient temperatures. There is strong evidence for a moment reordering transition at around 80 K which marks the crossover from a high polarization state ($T < 80$ K) to a more representative metallic ferromagnetic state ($T > 80$ K). The results from the different experimental techniques are successively reviewed, with special emphasis on the interplay between composition and electronic structure of the NiMnSb film surfaces. Surface segregation, consistent with a difference in free enthalpy between the surface and the bulk, is induced by annealing treatments. This surface segregation greatly reduces the surface polarization.

(Some figures in this article are in colour only in the electronic version)

1. Introduction

Half-metals, first postulated by de Groot in the early 1970s, can be considered as hybrids between metals and semiconductors, since the majority spin band structure shows a metallic behaviour, while the minority spin band structure exhibits a gap at the Fermi level such as in a semiconductor. Due to the gap for one spin direction, the density of states at the Fermi level has, theoretically, 100% spin polarization. Such fully spin polarized ferromagnetic materials are of considerable interest in the newly developed area of spin electronics (or spintronics). Among the most cited candidates for 100% spin polarization are the semi-Heusler alloys (NiMnSb) [1–9], full Heusler alloys [10, 11], zinc-blende structure materials [12–14], colossal magnetoresistance materials ($La_{1-x}Sr_xMnO_3$ [15, 16], Sr_2FeMoO_6 [17]), and semimetallic magnetic oxides (CrO_2 [18–21] and Fe_3O_4 [22, 23]). A number of other materials have also been suggested as half-metallic ferromagnets [24, 25].

NiMnSb was the first ferromagnet where half-metallic character at low temperature was predicted from band structure calculations [1]. Support for the half-metallic character of NiMnSb was significantly strengthened by the experimental studies of Hanssen *et al* [5], by comparing the angular correlations of positron annihilation with theoretical calculations. Numerous experimental efforts have, however, failed to prove the existence of full 100% polarization of conduction electrons at the Fermi level. All experiments performed to test the electronic properties near the surface lead to polarizations between 40 and 58% [26–31]. Nearly 100% polarization was reported on NiMnSb(100) sputtered thin films using spin polarized inverse photoemission [32–34]. However, these measurements were *k* resolved and therefore do not directly demonstrate the half-metallic character across the entire Brillouin zone. No claim was made that these measurements did indeed prove half-metallic character [32–34].

Several explanations have been put forward to account for the lower than expected polarization measured in [26–31]. First, it is known that at finite temperature, there exists a non-zero density of states in the minority channel due to magnons leading to a polarization lower than 100% [35–41]. Indeed, at any finite temperature, there will be electron–phonon and/or magnon–phonon coupling [36–38], or state rehybridization [41] so that polarization could decrease dramatically well below the Curie temperature. Other possibilities for significantly lower measured polarization could be related to the presence of spin minority surface states [9, 38, 42–46], surface segregation [32, 47, 48] or a variety of defects [31, 49, 50] which make the surface a different material from the bulk. Finally, the NiMnSb may not be a true half-metallic ferromagnet above 80 K [33, 41, 51, 52] though this would not explain the measured low polarization and magnetoresistance well below 80 K.

This paper presents experimental evidence that suggest that there are significant changes in electronic properties near a metamagnetic transition temperature of 80 K, far below the Curie point of NiMnSb ($T_C = 730$ K). At a temperature of about 80 K, there is a crossover from the high polarization metallic phase at lower temperatures to a more normal ferromagnet at higher temperatures is associated with a change in the magnetic moment and hybridization as a function of temperature. This summary of our experimental work, made on this system over the last six years, is now increasingly consistent with theoretical expectations [35–38, 41]. The structural, magnetic and electronic properties of the thin films, as well as their surfaces, suggests that a compelling experimental 'proof' of the half-metallic character remains elusive.

2. Epitaxy and morphology of the NiMnSb films on MgO substrates

NiMnSb(100) films have been deposited using a DC facing targets sputtering (FTS) system with three pairs of FTS (facing target sputtering) electrodes and one planar magnetron. More
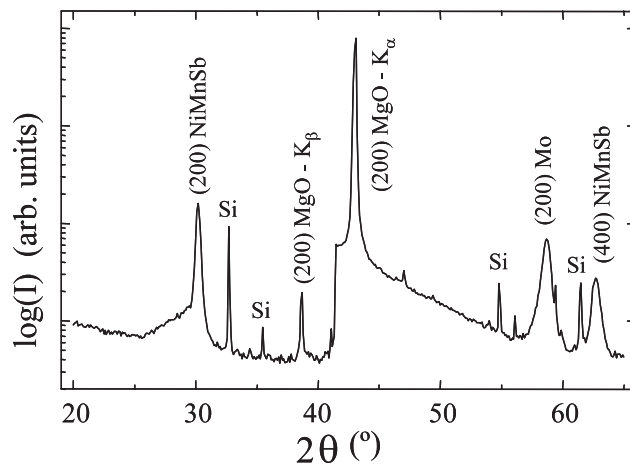
Figure 1. θ–2θ diffraction diagram for an NiMnSb 500 Å/Mo/MgO film deposited at 400 °C with $P_{Ar} = 10$ mTorr. The non-indexed peaks correspond to the Si sample holder. Adapted from [53].

details about the deposition process can be found in [53]. The main reason for exploiting FTS lies in the stoichiometric deposition which enables the use of a single 1:1:1 target. The chemically cleaned MgO monocrystalline (100) substrates were first baked for 2 h at 500 °C in order to remove the surface hydroxide layer and then set at the deposition temperature. A Mo seed layer was then sputtered with the planar magnetron at $P_{Ar} = 10$ mTorr with a deposition rate of 0.7 Å s^{-1} and a deposition temperature between 250 and 550 °C. Immediately after the deposition of the seed layer, the NiMnSb layer was sputtered at the same temperature and argon pressure, with a deposition rate of the order of 1 Å s^{-1}. A 150 Å Sb capping layer was finally deposited in order to prevent the any oxidation of the NiMnSb layer prior to introduction into ultrahigh vacuum for the surface science and electron spectroscopy studies. Deposition temperatures higher than 250 °C were used as NiMnSb growth on Si substrates exhibited poor crystallization for temperatures lower than 275 °C [54]. Rutherford backscattering (RBS) analysis indicated a 1:1:1 stoichiometry in all samples.

The crystalline structure and extent of crystallinity of the films were confirmed by means of θ–2θ of x-ray diffraction (XRD) as well as by grazing x-ray diffraction (GXRD), both using Cu Kα radiation. The XRD results in figure 1, for the range $20° < 2\theta < 65°$ from a film deposited at 400 °C, show only the (200) Mo peak and the (200) and (400) NiMnSb peaks. This indicates a strong (100) growth texture for both Mo and the NiMnSb. The same θ–2θ diagram was obtained for samples grown throughout the temperature range 350–650 °C. For deposition at temperatures higher than 550 °C, RBS analysis indicates that interdiffusion occurs at the Mo/NiMnSb interface. Complementary grazing x-ray diffraction (GXRD) experiments were performed to differentiate between simply textured films and real epitaxial growth. A GXRD diagram obtained on a 500 Å NiMnSb film deposited at 400 °C is presented in figure 2.

Clear evidence of epitaxy was found from GXRD, with epitaxial relationships of (100)NiMnSb/(100)Mo/(110)MgO. Such relative orientations are explained by considering the lattice parameters of MgO ($a_{MgO} = 4.213$ Å) and NiMnSb ($a_{NiMnSb} = 5.905$ Å), both presenting an fcc structure, and of Mo ($a_{Mo} = 3.147$ Å) presenting a bcc structure. As $\sqrt{2}a_{MgO} \approx 2a_{Mo}$ (with a misfit 5.2%), a rotation by 45° tilt is expected for Mo on MgO, whereas as $a_{NiMnSb} \approx 2.a_{Mo}$ (a misfit of 5.8%), so a cube on cube epitaxy is expected for NiMnSb on Mo. The schematic of the epitaxial relations between NiMnSb, Mo and MgO is
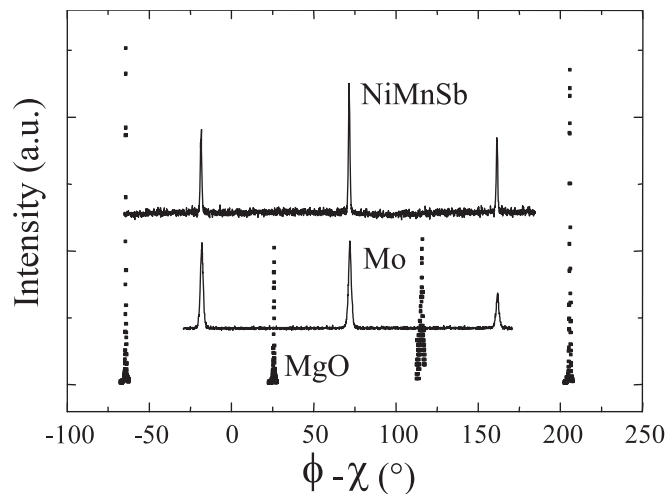
Figure 2. GXRD diagram of a NiMnSb 500 Å/Mo/MgO film deposited at 400 °C with $P_{Ar} = 10$ mTorr. Adapted from [53].
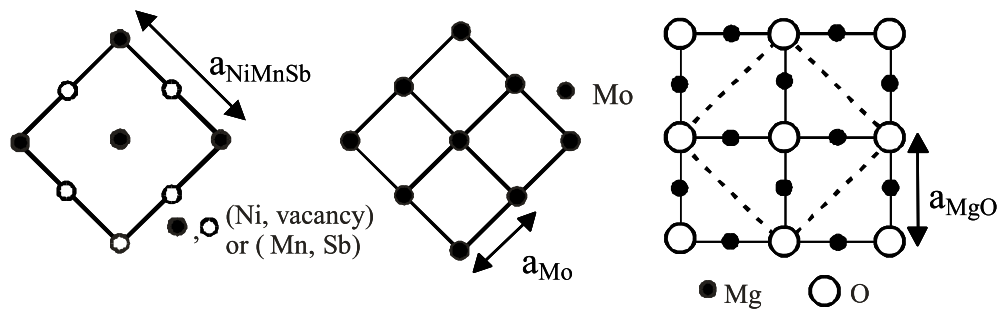

Figure 3. Schematic of the stacked epitaxial correspondences between NiMnSb, Mo and MgO, viewed in the (001) plane.

shown in figure 3 using the (001) projection. The mosaicity is found to be 1.5° for Mo and 2.5° for NiMnSb which indicates the rather good quality of the epitaxial growth. The Mo mosaicity is temperature independent, but in the case of NiMnSb the mosaicity was found to be larger for lower temperatures. Although MgO and NiMnSb present a smaller lattice mismatch ($\sqrt{2}.a_{MgO} \approx a_{NiMnSb}$, a misfit of 1%), NiMnSb grown directly on MgO exhibits (200) textured growth but the films were polycrystalline in all the temperature ranges studied. This is most likely due to the wetting (surface energy) of the MgO substrate, being more favourable for Mo buffer layer than for NiMnSb films.

The NiMnSb(100) surface morphology was investigated by atomic force microscopy (AFM) in contact mode. The AFM image of the Mo seed layer deposited at 400 °C is shown in figure 4. The Mo thin film surface is continuous and flat with an average roughness of 5 Å over a 10 μm^2 surface. The AFM image of an epitaxial NiMnSb film grown at 450 °C, under 10 mTorr of argon, is shown in figure 5(a). The film is discontinuous with rather flat islands (rms 5–7 Å) of square-like shapes and furrows along the [110] directions as deep as the film thickness. A tendency to percolation was observed with increasing thickness, although total percolation was not achieved in the thickness range studied here. To improve the surface quality and to
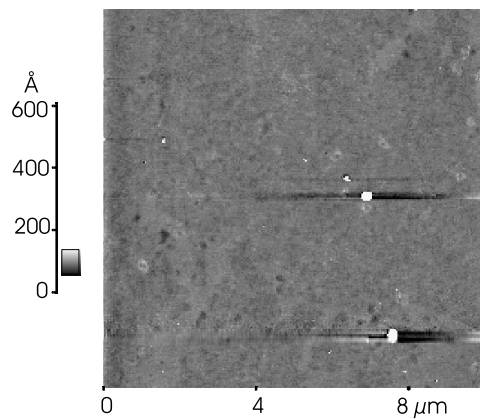
Figure 4. AFM image of a 10×10 μm^2 Mo/MgO surface deposited at $400\,^\circ$C. Adapted from [53].

achieve the necessary two-dimensional growth required for transport measurements as well as the surface and polarization studies, we varied the deposition temperature and Ar pressure (figures 5(b) and (c)). The optimum deposition conditions for NiMnSb on Mo appear to be $T = 400\,^\circ$C, $P_{\text{Ar}} = 3$ mTorr and a deposition rate of 0.6 Å s^{-1}. The AFM surface image of such a film shows an average roughness of about 8–9 Å (rms), has a mosaic spread of 2.3° and the film is fully continuous as presented in figure 5(d).

Increasing the growth temperature promotes the three-dimensional growth with better defined square islands. This can be understood by considering nucleation and growth thermodynamics [55]: the higher incident energy leads to a larger mobility of the adatoms and therefore to an island-like growth in the case of positive interface energy (as it appears to be the case here). High argon pressure also favours discontinuous growth (although not as dramatically as temperature) as generally observed for sputtered films [56]. Modest changes in the deposition rate, in the range studied here (0.5–1 Å s^{-1}), had no effect.

In order to ascertain the short range crystalline order in the NiMnSb films, we performed EXAFS (extended x-ray absorption fine structure) spectroscopy. The resulting oscillations of the measured absorption coefficient are characteristic of the chemical and structural environment of the absorbing atom. The short range three-dimensional NiMnSb thin film structure can be determined by fitting these oscillations. The EXAFS spectra were recorded at the D42 experimental station of the DCI storage ring at LURE, Orsay (France). Measurements were performed in the reflection mode, detecting the total electron yield (TEY) for probing the absorption coefficient above the K edges of Mn and Ni. The absorption spectra were normalized by the incident photon flux and performed using a Si(331) channel-cut monochromator.

The EXAFS measurements were performed using two geometries, i.e., with sample oriented parallel or perpendicular to the direction of the x-ray polarization vector, in order to probe the three-dimensional structure of the NiMnSb films. The overlap between the two L edges of Sb (L$_{\text{I}}$ and L$_{\text{II}}$) produced 'beating nodes' in the EXAFS oscillations, making the data analysis intractable for the Sb atom shell. Therefore, we limited our measurements to the Ni and Mn K edges. After background subtraction, the EXAFS oscillations were extracted and normalized to the height of the absorption step edge. The measured spectra were analysed using standard methods [57]. The theoretical EXAFS oscillations (amplitudes and phases) were calculated using McKale's method [58]. The fitting parameters were restricted to the number of atoms in the first coordination shell j (N_j), the distance between those atoms and the probed atom (R_j) and the Debye–Waller factors (σ_j).
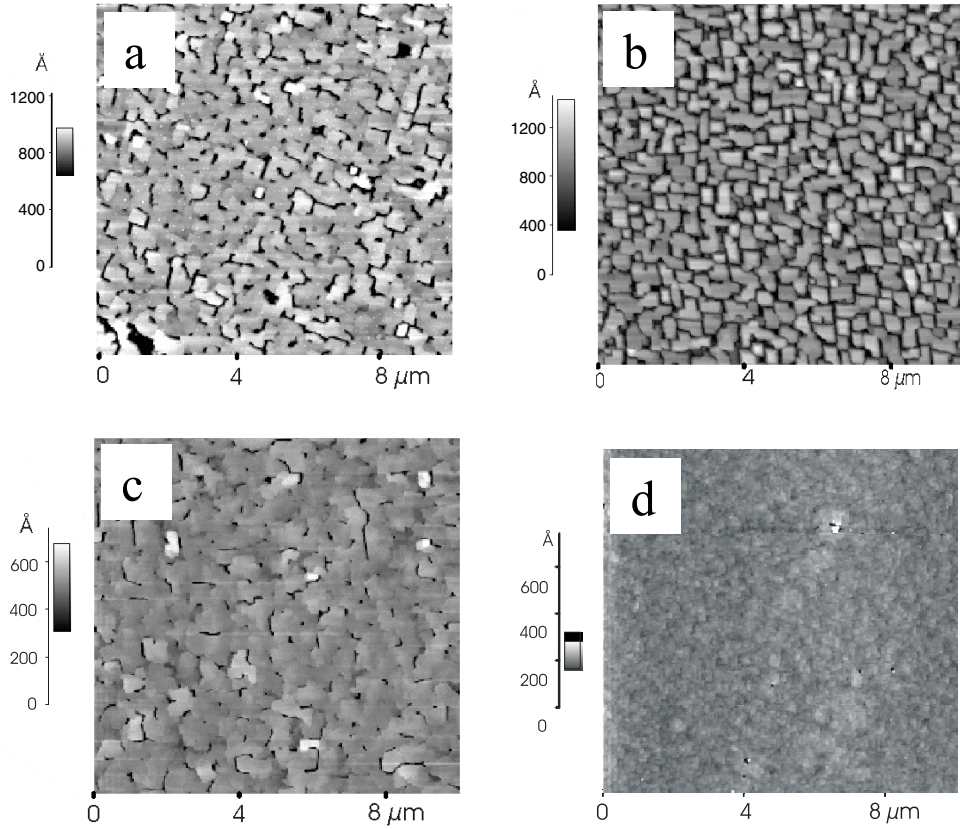
Figure 5. (a) AFM image of a $10 \times 10 \ \mu m^2$ surface of NiMnSb/Mo/MgO grown at $T = 450\,°C$ and $P_{Ar} = 10$ mTorr. (b) AFM image for $T = 550\,°C$ and $P_{Ar} = 10$ mTtorr. (c) AFM image for $T = 450\,°C$ and $P_{Ar} = 3$ mTorr. (d) AFM image for $T = 400\,°C$ and $P_{Ar} = 3$ mTorr. Adapted from [53].

In the case of a perfect NiMnSb structure, a Mn atom has four Ni atoms in the first coordination sphere at a distance of $\frac{a\sqrt{3}}{4} \cong 2.55$ Å and, in a second coordination sphere, six Sb atoms at a distance of $\frac{a}{2} \cong 2.95$ Å, where $a = 5.9$ Å is the lattice parameter of NiMnSb. The EXAFS simulations were performed with two coordination spheres about Mn, the first one containing Ni atoms and the second one Sb atoms, and with the corresponding phase $\varphi_j(k)$ and amplitude $F_j(k)$ functions, as indicated by a continuous line in figure 6 for (a) the parallel and (b) the perpendicular configurations. The Ni atom is surrounded at equal distance of $\frac{a\sqrt{3}}{4} \cong 2.55$ Å, by four Mn atoms and four Sb atoms. We were forced to use two coordination shells for the simulation of the data from Ni, since the code used does not accept two atomic species situated in the same shell, and the fittings to the data are shown in figure 7 (the continuous lines). For both Mn and Ni, there is good agreement between experimental and calculated k-weighted amplitudes for both (a) the parallel and (b) the perpendicular configurations. For the data from Mn, the calculated Debye–Waller factors are 0.06 for Ni and 0.065 for Sb, while for the EXAFS data from Ni, the Debye–Waller factors are 0.062 for the Mn atoms and 0.058 for the Sb atoms.

The agreement in bond lengths and shell occupation, between theoretical values and those abstracted from the EXAFS data, as summarized in table 1 for the coordination spheres about
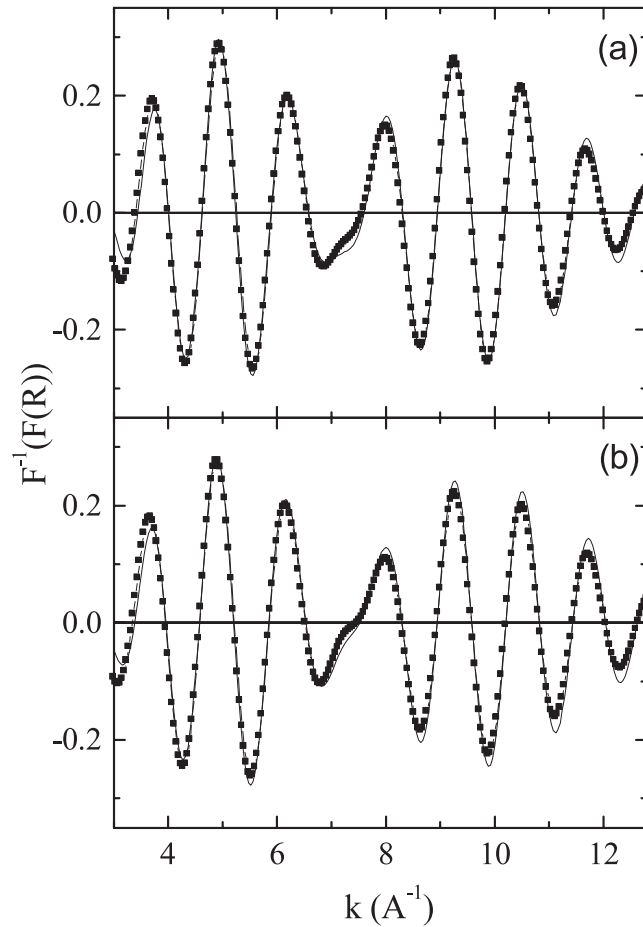
Figure 6. *k*-weighted EXAFS spectra recorded at the Mn edge in parallel (a) and perpendicular (b) configurations. The solid lines correspond to the simulations of the NiMnSb structure while the dots represent the experimental measured spectra. Adapted from [34].

Table 1. Results for the simulations of the EXAFS spectra at the Mn edge for the two configurations. Adapted from [34].

	N_{Ni}	R_{Ni} (Å)	N_{Sb}	R_{Sb} (Å)
Parallel	3.98 ± 0.24	2.54 ± 0.27	6.01 ± 0.30	2.97 ± 0.21
Perpendicular	3.61 ± 0.27	2.55 ± 0.28	5.98 ± 0.31	2.95 ± 0.21
Theory	4	2.55	6	2.95

Mn and in table 2 for the coordination spheres about Ni, indicates that the short range atomic order is excellent. A small disagreement between calculated and experimental spectra in the parallel compared to the perpendicular configuration can be seen in figure 6, especially near $k \cong 7$ Å^{-1}. However, the resulting parameters shown in table 1 do not change significantly along the two directions, which suggests that possible lattice deformations, such as those induced by the substrate, are very weak. For Ni, the measured oscillations do not match expectations very well at small values of *k* (characteristic of longer distances), the fittings are
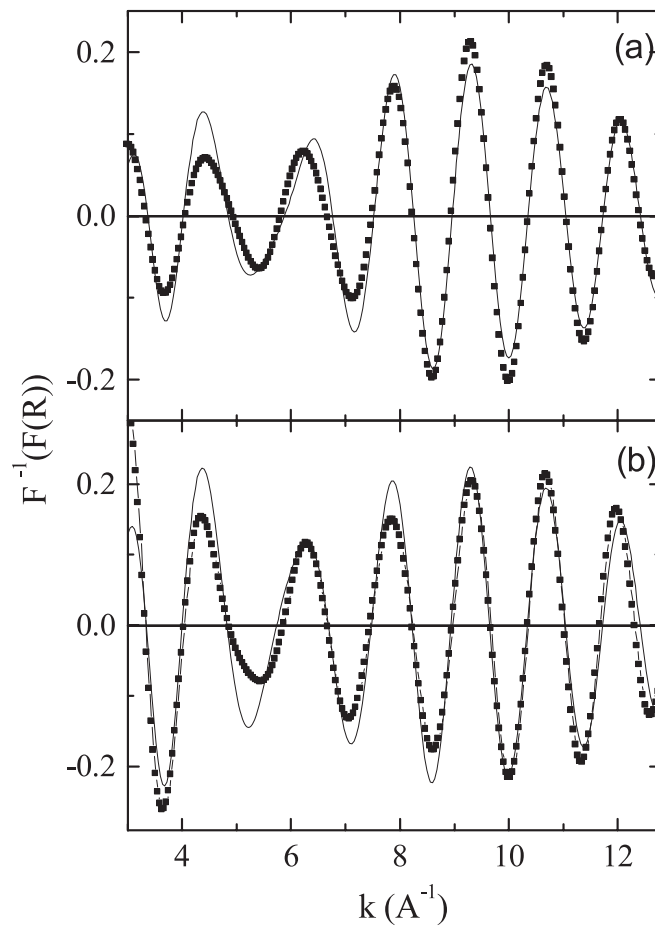
Figure 7. *k*-weighted EXAFS spectra recorded at the Ni edge in parallel (a) and perpendicular (b) configurations. The solid lines correspond to the simulations of the NiMnSb structure while the dots represent the experimental measured spectra. Adapted from [34].

Table 2. Results for the simulations of the EXAFS spectra at the Ni edge for the two configurations. Adapted from [34].

	N_{Mn}	R_{Mn} (Å)	N_{Sb}	R_{Sb} (Å)
Parallel	3.88 ± 0.47	2.53 ± 0.07	3.51 ± 0.59	2.57 ± 0.06
Perpendicular	3.98 ± 0.13	2.54 ± 0.20	3.85 ± 0.61	2.56 ± 0.17
Theory	4	2.55	4	2.55

better match in position and intensity for higher *k* values, and the fit improves significantly. Note that the calculated spectra do not change shape and position when the Mn atoms and Sb atoms are interchanged in the first coordination shell about Ni.

To summarize, the EXAFS measurements showed that our NiMnSb films grown at 400 °C on Mo buffer layers exhibited good short range crystalline order, adding further support to the assertion that our NiMnSb(100) films are of high quality. The relatively elevated lattice mismatch of 5.8% between NiMnSb and Mo films is accommodated in the first few monolayers
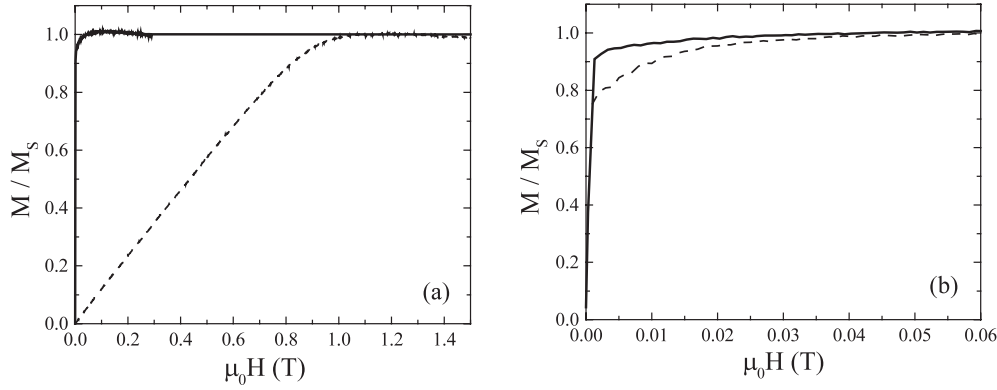
Figure 8. (a) 10 K virgin magnetization curves of an Mo 50 Å/NiMnSb 1000 Å/Mo 100 Å trilayer deposited in the optimal conditions of figure 5(d), with the applied field parallel (full line) and perpendicular (dotted line) to the film plane. (b) In-plane virgin magnetization curves with the applied field parallel to the (100) (full line) and (110) (dotted line). Adapted from [53].

of the NiMnSb layer, whose total thicknesses ranged from 500 to 1000 Å. The use of high quality thin films, rather than bulk single crystals is essential for the spin polarized electron spectroscopy measurements described later. Given the constraints necessary for careful surface characterization, transport measurements and polarization studies, only films grown under optimal conditions of figure 5(d) were used for the measurements described later.

3. Magnetic and transport properties of the NiMnSb films

Initial insight into the magnetic properties of crystalline NiMnSb films can be obtained from analysis of magnetic and transport properties, as a function of temperature. The magnetic measurements were measured with vibrating sample magnetometer (VSM) between 1.5 and 300 K and ferromagnetic resonance measurements were performed at RT on a standard X band Bruker spectrometer. Transport measurements were also undertaken between 1.5 and 300 K in the conventional AC four-point probe geometry on the NiMnSb films with typical thicknesses of 500–1000 Å.

The virgin magnetization curves of a 1000 Å thick film, measured at 10 K in an applied field, with the parallel and perpendicular components presented in figure 8. The magnetization clearly lies in the film plane with an out of plane anisotropy of 0.9 T. Assuming that this anisotropy is due solely to shape anisotropy ($H_A = 4\pi M_s$), then a magnetic moment per Mn atom of $3.9 \pm 0.2\ \mu_B$ is deduced. This value is consistent with the expected value of $4.0\ \mu_B$ per formulae unit determined from ground state band structure calculations [1] and with the value measured on bulk single crystals by polarized neutron diffraction ($3.98 \pm 0.03\ \mu_B$ per formulae unit [48], as discussed later). Regrettably, this does not prove half-metallic character as this is not a zero-field measurement, and an increase in spin wave stiffness is expected with high magnetic fields [37, 60]. Also the uncertainly in the measurement does not make it possible to exclude correlation effects (i.e. a non-quasiparticle density of states) [61, 62] that can limit polarization from reaching 100% in a small way in the ground state.

The in-plane magnetic anisotropy was investigated both by conventional magnetometry (VSM) and by ferromagnetic resonance. As a fourfold symmetry is expected in cubic crystals, the virgin magnetization curves were measured with the field along the (100) and (110) crystallographic directions (figure 8(b)). The (110) axis appears to be the hard axis with a
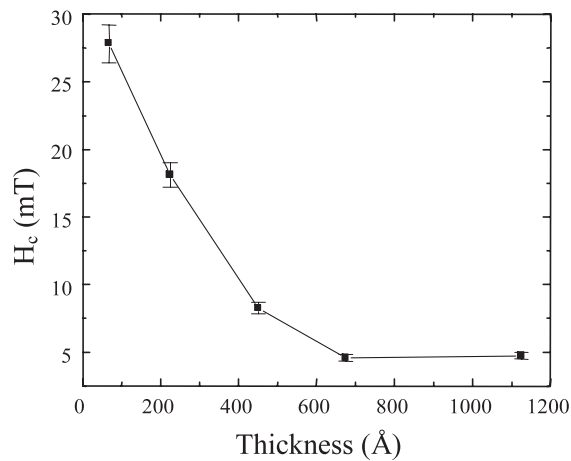
Figure 9. Evolution of the coercive field as a function of film's thickness, at room temperature. Adapted from [53].
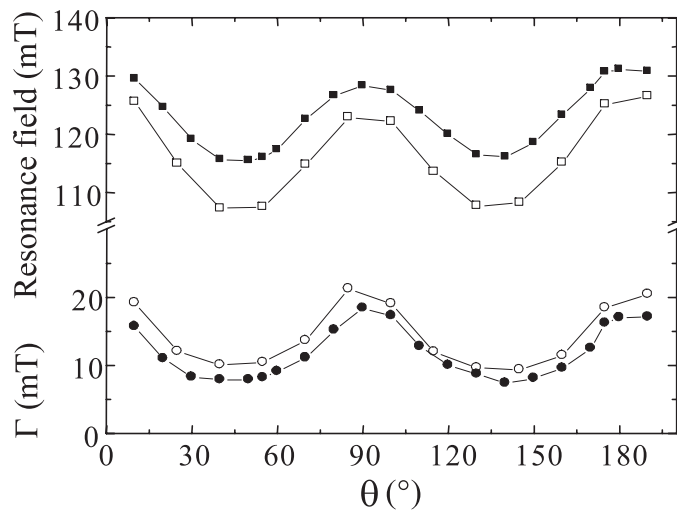

Figure 10. Resonance field (top) and linewidth (bottom) as a function of angle θ between the applied field and the (110) axis, at 300K (full symbols) and at 10 K (empty symbols). Adapted from [34].

corresponding anisotropy field of 25 ± 2 mT. The coercive field, shown in figure 9, varies from 5 to 30 mT, in an inverse relationship with the film thickness—the thinner the film, the bigger the coercive field, a common phenomena in thin ferromagnetic films which can occur due to trapping of the coercive field by the surface imperfections or by surface oxidation as the layer thickness gets very small.

The evolution of the FMR resonance field as a function of the in-plane angle θ with the (110) axis is summarized in figure 10, for films at both 300 K (filled symbols) and at 10 K (open symbols). The (100) easy axis and the fourfold anisotropy are clearly evident, with a deduced anisotropy field of 20 ± 2 mT at 10 K, in good agreement with the value obtained from static measurements, of 25 mT also at 10 K. The linewidth follows the same angular dependence
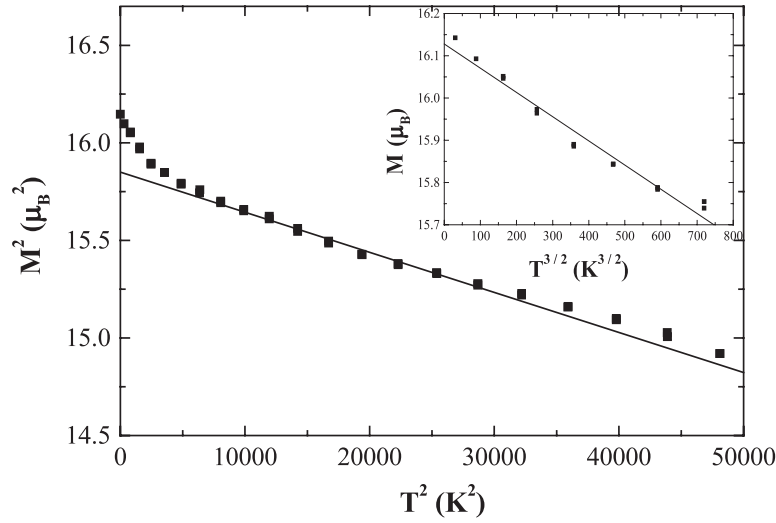
Figure 11. Temperature dependence of the magnetization for $T > 100$ K and as an inset, for $T < 100$ K. Adapted from [53].

as the resonance field, with small overall values (10–20 mT) which indicates good magnetic homogeneity.

The temperature dependence of the magnetization along the (110) axis below 200 K is illustrated in figure 11. Above 100 K, M^2 varies linearly as a function of T^2, whereas a deviation from the T^2 law appears for temperatures lower than 100 K, where the magnetization varies more rapidly ($\sim T^{3/2}$). Such a behaviour is identical to what has been observed in bulk single crystals and is ascribed to a transition from a low temperature localized ferromagnetism in which collective spin wave excitations predominate (as expected for a nominal half-metal or very high polarization ferromagnet) to a high temperature itinerant-like ferromagnetism in which spin fluctuations contribute to the decay of the net moment [51]. The very existence of spin waves at lower temperatures, assuming the model [51] is correct, precludes ideal (100% polarization) half-metallic character [24, 45].

The temperature dependence of the resistivity, after the subtraction of the Mo buffer layer contribution, is shown in figure 12, again for a 1000 Å NiMnSb epitaxial film deposited in the optimal conditions described in section 2. The extrapolated residual resistivity is 5.3 $\mu\Omega$ cm, which is lower than the best values reported for polycrystalline thin films ($\sim$20 $\mu\Omega$ cm) and polycrystalline bulk samples (6.9 $\mu\Omega$ cm) [63], and consistent with the high quality of our films. A kink in the temperature dependence of the resistivity occurs around 70 K, which has been already observed in NiMnSb polycrystalline film and bulk samples [51, 63, 64]. For temperatures lower than 70 K the resistivity obeys a T^2 law: $R(T) = R_0 + AT^2$ with $R_0 = 5.3$ $\mu\Omega$ cm and $A = 5.8 \times 10^{-4}$ $\mu\Omega$ cm K^{-2}, while at higher temperatures $R(T) = R_0' + A'T^{1.65}$ with $R_0' = 6.1$ $\mu\Omega$ cm and $A' = 1.7 \times 10^{-3}$ $\mu\Omega$ cm K$^{-1.65}$. As it is more and more difficult to extract the resistivity of the NiMnSb layer in the Mo/NiMnSb/Mo trilayer when its thickness is reduced (the parallel resistor model is no longer strictly valid), we have plotted the room temperature resistance versus the inverse of the film thickness (figure 13). A linear behaviour is observed which indicates a thickness independent resistivity in the thickness range studied here (100–1000 Å). The slope of the linear fit yields the average room temperature NiMnSb resistivity of 19.9 $\pm$ 1.5 $\mu\Omega$ cm.
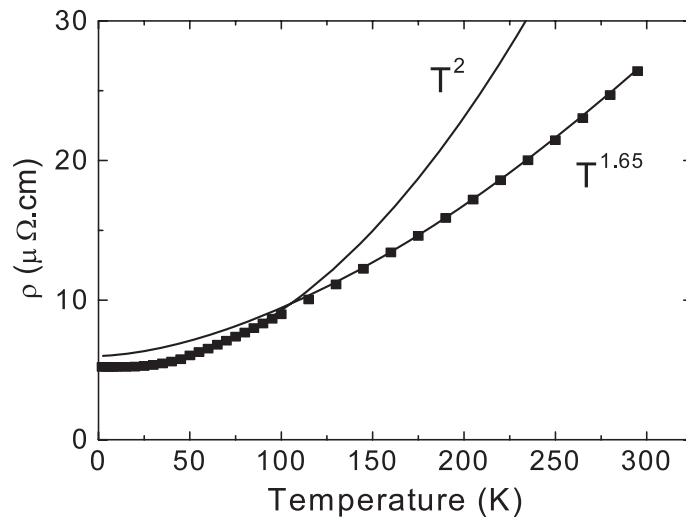
Figure 12. The thermal variation of the resistivity for a 1000 Å thick NiMnSb film. Adapted from [34, 53].
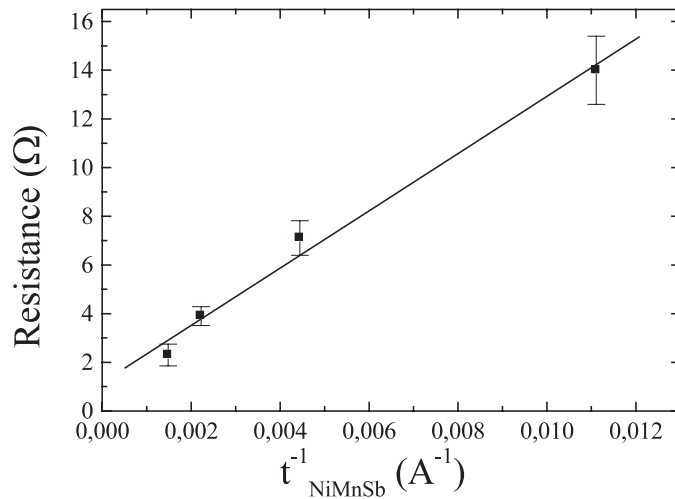

Figure 13. Thickness dependence of the overall resistance in Mo/NiMnSb(t)/Mo trilayers deposited in the optimal conditions of figure 5(d). Adapted from [53].

4. Characterization of the surface composition

The question 'what is a surface' can be answered in many ways depending on the significance of the property studied. In a strictly physical sense, it is the outermost, top monatomic layer of a solid. Since it is now well known that equilibrium segregation can exist at the surface or in some cases extending to a many atomic layers away from the surface, the study of surface composition is necessary in any compound or alloy system before one can assess the value of spin polarization. We adopted angle resolved x-ray photoemission (ARXPS) as the most expedient technique for characterizing the surface composition of half-metals and related compounds.
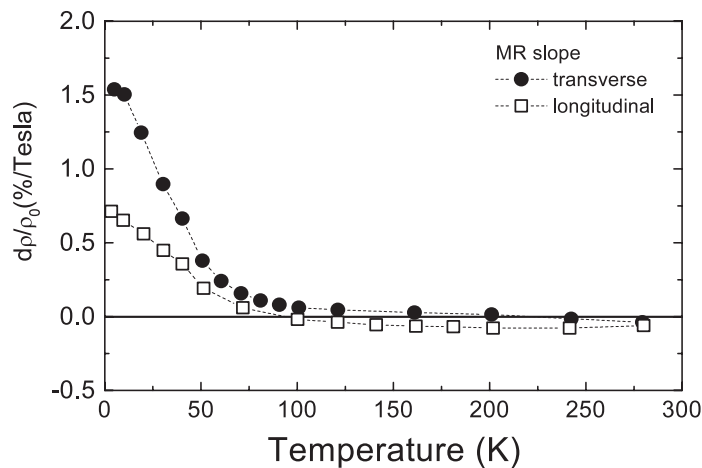
Figure 14. Transverse and longitudinal MR in NiMnSb films (slopes of MR curves between 1 and 6 T). Adapted from [52].
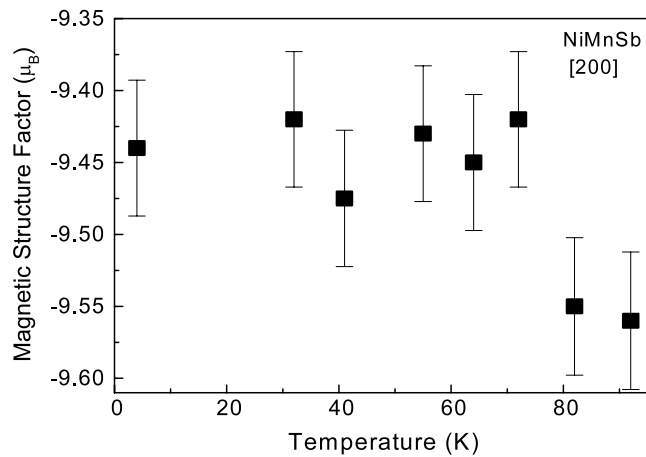

Figure 15. The temperature dependence of the magnetic structure factor for the ⟨200⟩ peak obtained from neutron diffraction. Adapted from [33, 59].

To excite the core level photoelectrons, we used an x-ray source with an Mg anode having the main Mg $K_{\alpha1,2}$ line at 1253.6 eV with the full width at half-maximum of 0.65 eV. We used a hemispherical electron energy analyser from Physical Electronics (PHI Model 10-360 Precision Energy Analyzer), with 8.5 inch radius. The combined resolution of the x-ray source and analyser was 650 meV.

In ARXPS, the surface composition can be determined with great accuracy since the effective probing depth becomes shorter as the emission angle is increased with respect to the surface normal. The experimental core level intensities for any two components from a multicomponent alloy are acquired at several emission angles θ, usually from $\theta = 0°$ (normal emission) to 60° (off-normal emission). Then, a linear background contribution is systematically subtracted from each raw spectrum. The peak intensities are further normalized by the corresponding differential cross section for emission and by the analyser transmission function [48, 65–68]. The experimentally normalized intensity ratio for any two elements A

and B is thus given by:

$$R^{\text{exp}}(\theta) = \frac{I(\text{A})/\sigma_\text{A}}{I(\text{B})/\sigma_\text{B}} \frac{T(E_\text{A})}{T(E_\text{B})} \qquad (1)$$

where $I(\text{A})$ and $I(\text{B})$ are the measured core level intensities for elements A and B, σ_A and σ_B are the cross sections, and $T(E_\text{A})$ and $T(E_\text{B})$ are the transmission functions of the analyser for elements A and B as a function of the corresponding photoelectron kinetic energies E_A and E_B and are based on the measured transmission functions for each analyser. For example, in our case, the transmission function of PHI 10-360 Precision Energy Analyzer is $T(E_\text{A}) = \sqrt{E_\text{A}}$ [69].

Over the past decades, the phenomenon of surface segregation attracted quite a lot of theoretical interest. Up to now, various theories have been developed in order to account for the enrichment at the binary alloy surface. The first-principles approach [70], embedded atom method (EAM) model [71], Finnis–Sinclair (FS) potential [72], and Bozzolo–Ferrante–Smith (BFS) method [73] have been used to simulate the surface segregation for fcc type random and ordered alloys, while for fcc and hcp elements the modified analytic embedded atom method (MAEAM) many-body potential is used to theoretically study the surface segregation phenomena of binary alloys [74]. Unfortunately, to our knowledge, there are no detailed theoretical studies of the surface segregation of multicomponent half-metal alloys, although there are now some studies of the NiMnSb(100) surface stability [38, 42, 44, 75, 76]. We use here a simplified model to fit the experimental intensity ratios obtained from ARXPS.

The comparison between theory and experiment is accomplished through considerations of the theoretical normalized intensity ratio of element A and B as given by:

$$R^{\text{theor}}(\theta) = \frac{\sum_{j=0}^{\infty} f_j(\text{A}) \exp\left[\frac{-\text{j}d}{\lambda_\text{A}^j \cos(\theta)}\right]}{\sum_{j=0}^{\infty} f_j(\text{B}) \exp\left[\frac{-\text{j}d}{\lambda_\text{B}^j \cos(\theta)}\right]} \qquad (2)$$

where λ_A^j and λ_B^j are the inelastic mean free paths of the core electrons generated from elements A and B respectively and passing through the material contained in layer j. The inelastic mean free paths can be adopted from previously published methodologies [77] contained within the NIST Electron Inelastic Mean Free Path program [78]. The atomic fraction of element A (chosen as the element which segregates to the surface) in the jth layer below the surface is given by:

$$f_j(\text{A}) = b + \delta \exp(-\text{j}d/G) \qquad (3)$$

where b is the bulk fraction of element A, δ and G are fitting parameters representing the extent of the segregation and the segregation depth respectively, and d is the distance between atomic layers. These two quantities are also the fitting parameters when comparing the model with experimental values. From the profile form $f_j(\text{A})$ one can calculate the apparent surface concentration (or relative intensity) of element A for a particular core level.

Considering now the case of the NiMnSb films, three sublattices correspond to a given atom respectively (Ni, Mn and Sb) whilst the fourth is empty. In this crystallographic structure, the (001) surface of NiMnSb is binary, composed of alternate planes of {Mn, Sb} and {Ni, vacancy}. If the surface free energy is different from the bulk, substantial segregation may appear on the surface, disturbing both the crystalline and electronic structures in that region.

The NiMnSb epitaxial films were protected with a 1000 Å of Sb capping layer to prevent oxidation and surface disorder. The Sb layers were removed in UHV, without destroying the NiMnSb surface, by application of a 'flash' thermal treatment which resulted in rapid Sb sublimation. Moreover, this treatment limits the possible thermal activated segregation to a minimum. The thermal treatment involved resistive heating of the sample up to 400 °C for
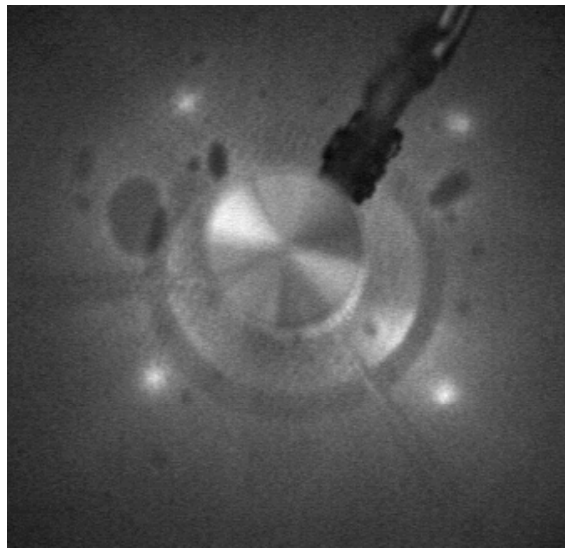
Figure 16. The LEED pattern of a stoichiometric ordered NiMnSb surface obtained through annealing the sample to 400 °C. Adapted from [32].

several minutes, followed by a fast cooling to room temperature. No evidence of surface Sb diffusion into the NiMnSb bulk was found in the angle resolved XPS surface characterization studies described below and such Sb diffusion is unlikely in any case due to reduced melting temperature of Sb compared to NiMnSb. Once the Sb capping layer was removed, the crystallinity and orientation of the stoichiometric NiMnSb(100) surface was again established using low energy electron diffraction (LEED). Figure 16 shows a LEED image recorded at room temperature, using 34 eV incident electron energy, for the stoichiometric surface obtained after removal of the Sb capping layer.

The fourfold low energy electron diffraction images exhibited very sharp spots, indicative of an ordered surface region. Knowing the geometry and dimensions of the LEED system, the surface lattice constant was extracted from equation:

$$2a \sin \theta = n\lambda, \qquad \lambda = \frac{h^2}{\sqrt{2mE_{\mathrm{kin}}}} \tag{4}$$

where $n = \sqrt{h^2 + k^2}$ for a square lattice, E_{kin} is the kinetic energy of the incident electrons, and $\sin \theta$ can be calculated from the geometry of the measurement. The distance between the central spot (not shown in figure 16) and any of the fourfold-symmetric spots corresponds to the Mn–Mn or equivalently, Sb–Sb distance of 4.24 Å in the real space. The surface thus prepared can be considered a proper termination of the bulk NiMnSb, consistent with the angle resolved XPS described below. The lifetime of the surface is limited by carbon contamination to several hours.

The terminal layer of the thin film was determined using angle resolved photoemission and the fitting procedures introduced above. The core levels with the highest cross section for each atomic species have been monitored at room temperature $-2p_{1/2}$ and $2p_{3/2}$ for Mn, $3d_{3/2}$ and $3d_{5/2}$ for Sb, $2p_{3/2}$ for Ni. Surface contributions to the peak intensities are enhanced at high emission angles, whereas bulk contributions dominate at normal (0° with respect to the surface normal) emission, as can be seen in figure 17. The angular resolution of the acquired ARXPS spectra was 2°, smaller than the acceptance angle of the analyser. The first observation that can
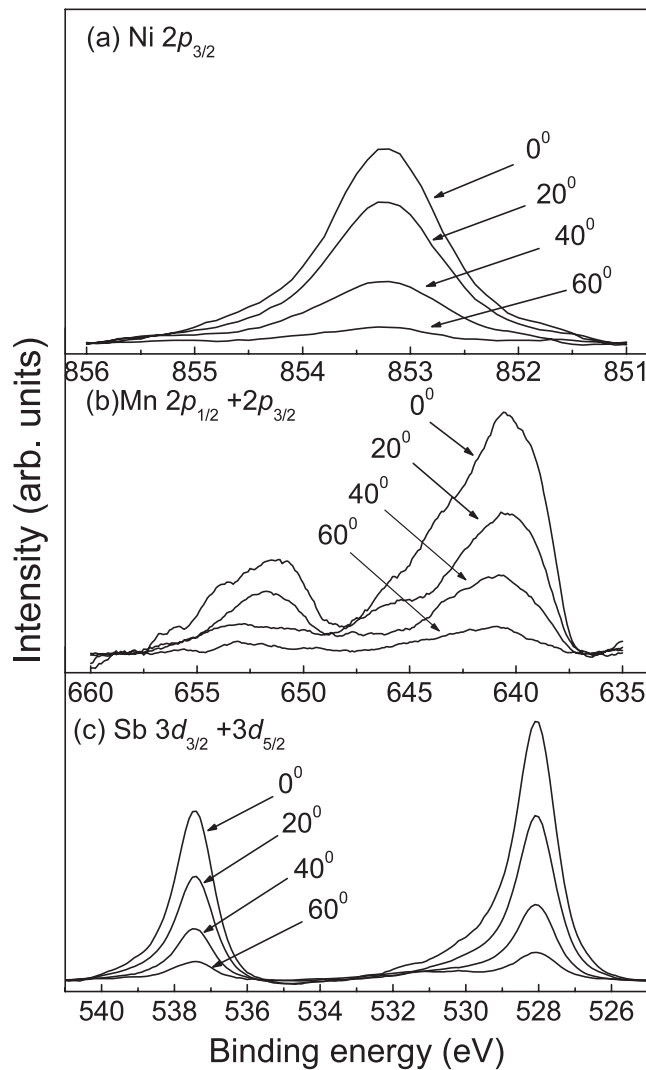
Figure 17. The Ni $2p_{3/2}$ (a), Mn $2p_{3/2} + 2p_{1/2}$ (b), and Sb $3d_{5/2} + 3d_{3/2}$ (c) core levels of NiMnSb are shown as a function of emission angle. Emission along the surface normal is the spectrum labelled with 0°. Adapted from [48].

be drawn from this figure refers to the shape of all spectra, which are very well defined and free of satellites. The presence of satellites near the main photoemission peaks would be indicative of either strong core–hole interactions (as is the case in CMR perovskites [66]) or the presence of more than one equivalent crystallographic site for the same atomic species.

The increase in the Mn $2p_{3/2}$ halfwidth is consistent with the placement of Mn in a more metallic environment in half-metallic NiMnSb than is the case in the half-metallic manganese perovskites, as well as because of the multiplicity of the final states possible, including a surface to bulk core level shift, and has been observed before for other cubic compound pnictide systems [79]. Concerning the core level peak positions, the binding energy corresponding to each core level matches the values reported in the literature [80], as summarized in table 3.
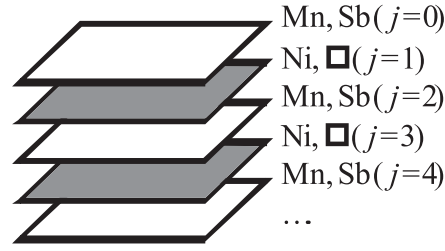
Figure 18. Layer stacking sequence assumed for the stoichiometric surface.

Table 3. Comparison between the binding energies obtained experimentally and the values published in [80].

	Ni $2p_{3/2}$ (eV)	Mn $2p_{3/2}$ (eV)	Mn $2p_{1/2}$ (eV)	Sb $3d_{5/2}$ (eV)	Sb $3d_{3/2}$ (eV)
Exp. values	853.2 ± 0.1	640.1 ± 0.1	651.0 ± 0.1	528.1 ± 0.1	537.5 ± 0.1
Reference [80]	853.3	639.4	650.6	528.2	537.7

At last, it is important to note that, apart from Mn, the positions of the photoelectron peaks in figure 17 do not depend on emission angle, which indicates that the valence state of the atoms in the surface is the same as the chemical environment deeper in the bulk, neglecting issues related to the surface to bulk core level shift associated with the Mn 2p which suggest that Mn occupies the surface terminal layer. We can determine the surface stoichiometry by fitting specific angle resolved XPS intensity ratios with a theoretical model based on the naturally layered structure of NiMnSb. As indicated in figure 18, we start by assuming that the Heusler alloy structure consists of alternating layers of {Mn, Sb} and {Ni, vacancy}, spaced at a distance of 1.5 Å. The stoichiometric crystal must be terminated by either a {Mn, Sb} or a {Ni, vacancy} plane. We also considered the possibilities of atomic disorder in the Ni vacancy planes resulted from the replacement of the vacancy site by Mn, Sb or Ni.

Different core level intensity ratios are plotted against emission angle in figure 19. Each raw spectrum was analysed by first subtracting a linear background and then normalizing with the corresponding cross section values from [81], as well as with the analyser transmission function. The model calculations presented as lines in figure 19 are obtained from summing over each layer contributing to the photoemission signal. This can be translated by attributing an index j for each atomic plane and then summing over odd or even values of j in equation (4). The experimental data in figure 19 are compared to several models for the surface termination including (I) {MnSb}(surface)/[Ni, vacancy/Mn, Sb]$_n$ which represents the case of a perfect ordered crystal, and (II) {Ni, Mn}(surface)/[Mn, Sb/Ni, vacancy]$_n$ and (III) {Ni, Sb}(surface)/[Mn, Sb/Ni, vacancy]$_n$, which represent the case of the replacement of the vacancy site by a Mn or Sb atom, respectively.

For example, in model (I), the Mn and Sb atoms are assumed to be in even layers (j = even), while the Ni atom is in odd layers (j = odd). The elemental ratios can be written as:

$$\frac{I(\text{Mn})}{I(\text{Sb})} = \frac{\sum_{j=0}^{\infty} 0.5 \exp\left(-\frac{2j}{\lambda_{\text{Mn}} \cos\theta}\right)}{\sum_{j=0}^{\infty} 0.5 \exp\left(-\frac{2j}{\lambda_{\text{Sb}} \cos\theta}\right)} = \frac{1 - \exp\left(-\frac{2}{\lambda_{\text{Sb}} \cos\theta}\right)}{1 - \exp\left(-\frac{2}{\lambda_{\text{Mn}} \cos\theta}\right)}, \tag{5}$$

$$\frac{I(\text{Ni})}{I(\text{Sb})} = \frac{\sum_{j=0}^{\infty} 0.5 \exp\left(-\frac{2j+1}{\lambda_{\text{Ni}} \cos\theta}\right)}{\sum_{j=0}^{\infty} 0.5 \exp\left(-\frac{2j}{\lambda_{\text{Sb}} \cos\theta}\right)} = \exp\left(-\frac{1}{\lambda_{\text{Ni}} \cos\theta}\right) \frac{1 - \exp\left(-\frac{2}{\lambda_{\text{Sb}} \cos\theta}\right)}{1 - \exp\left(-\frac{2}{\lambda_{\text{Ni}} \cos\theta}\right)}, \tag{6}$$
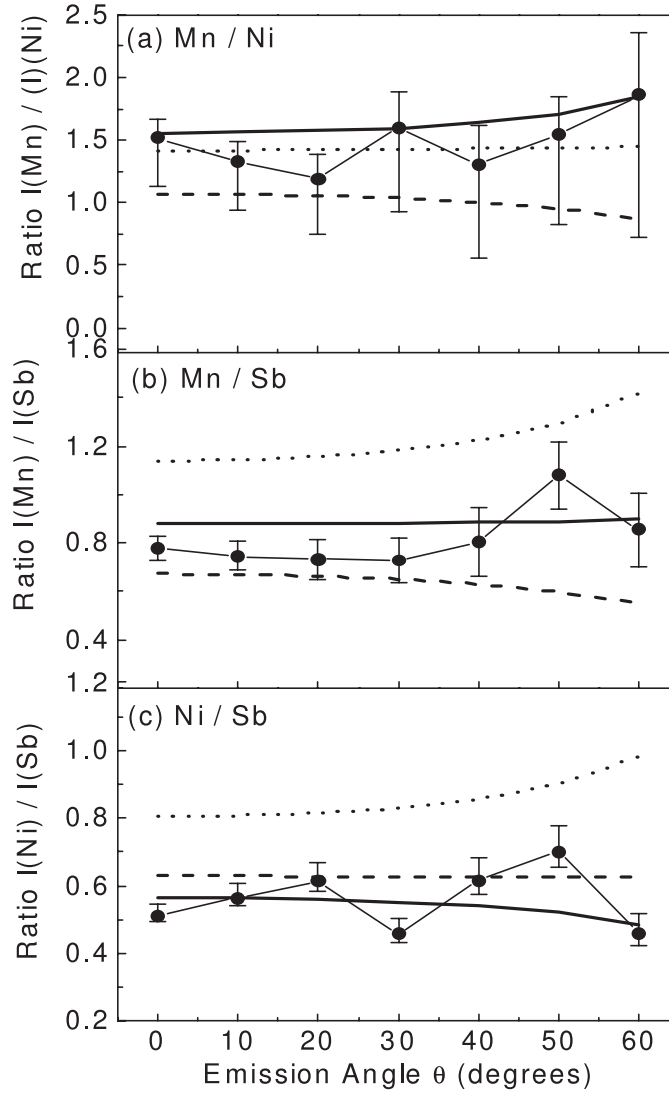
17

Figure 19. Angle resolved photoemission intensities ratios of the Ni $2p_{3/2}$, Mn $2p_{3/2} + 2p_{1/2}$, and Sb $3d_{5/2} + 3d_{3/2}$ core levels of NiMnSb following the removal of excess Sb with a 700 K flash anneal (circles). The data are compared to several models for surface termination including the stoichiometric alloy {MnSb}(surface)/[Ni, vacancy/Mn, Sb]$_n$ (I continuous line), {Ni, Mn}(surface)/[Mn, Sb/Ni, vacancy]$_n$, (II dotted line) and {Ni, Sb}(surface)/[Mn, Sb/Ni, vacancy]$_n$ (III dashed line). Adapted from [32, 48].

$$\frac{I(\mathrm{Mn})}{I(\mathrm{Ni})} = \frac{\sum_{j=0}^{\infty} 0.5 \exp\left(-\frac{2j}{\lambda_{\mathrm{Mn}} \cos \theta}\right)}{\sum_{j=0}^{\infty} 0.5 \exp\left(-\frac{2j+1}{\lambda_{\mathrm{Ni}} \cos \theta}\right)} = \exp\left(\frac{1}{\lambda_{\mathrm{Ni}} \cos \theta}\right) \frac{1 - \exp\left(-\frac{2}{\lambda_{\mathrm{Ni}} \cos \theta}\right)}{1 - \exp\left(-\frac{2}{\lambda_{\mathrm{Mn}} \cos \theta}\right)}, \tag{7}$$

where the λs are the effective mean free paths corresponding to each core level measured, and θ is the emission angle. The other two models (II and III) shown in figure 19 assume Ni atoms in the even layers (j = even) and Mn/Sb in the odd layers (j = odd). The fits resulted from these three models give poor agreement with the measured intensity ratios.
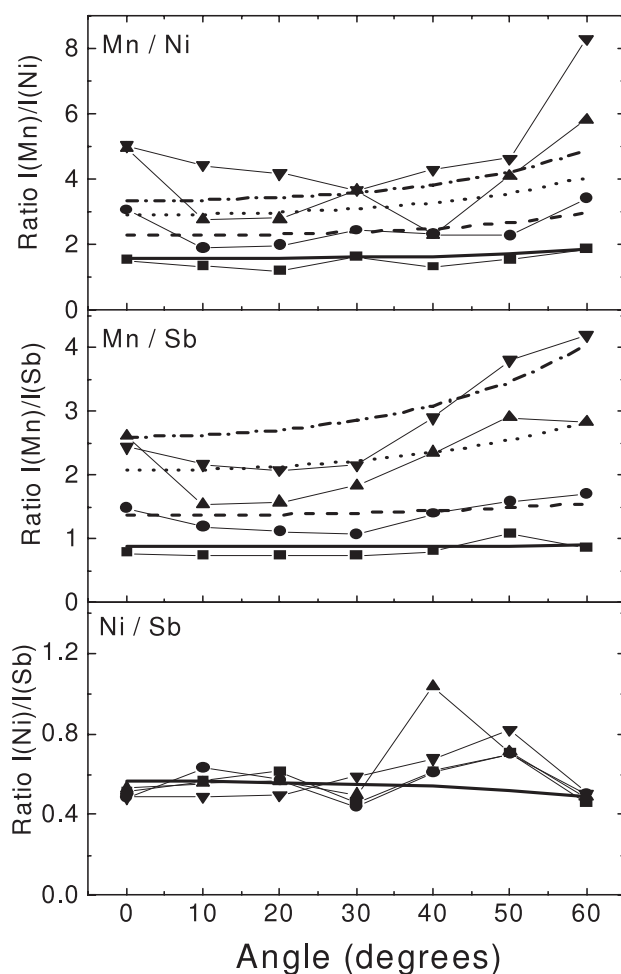
Figure 20. The angle resolved x-ray photoemission intensity ratios of the Ni $2p_{3/2}$, Mn $2p_{3/2}$, and Sb $3d_{5/2}$ core levels of NiMnSb. The data are compiled from spectra taken as a function of emission angle following removal of the excess Sb with a 700 K anneal (squares) and following continued sputtering and annealing cycles of 10 min (circles) followed by 1/2 h (up-triangles) and finally by 1 h (down-triangles) total annealing times. The data points are fitted with a segregation model in which Mn atoms migrate to both vacancy sites as well as replace Sb and Ni atoms from their lattice sites in the surface region except for data for the surface stoichiometric alloy termination Sb(surface):Ni:(MnSb:Ni)$_n$ shown with continuous line. Adapted from [48].

The best fit, shown as a continuous line in figure 19, was obtained by the model with a {Mn, Sb}(surface)/[Ni, vacancy/Mn, Sb]$_n$ layered structure.

The electron mean free paths used in the above equations are adapted from calculations of Penn in [82]. The approximation needed in calculating the λs is dictated by the fact that each photoelectron must travel through a selvedge region with unknown relative density before escape into vacuum. We considered an average value for the mean free path of each element monitored, as calculated in table 4. For example, a Mn $2p_{3/2}$ photoelectron, at 613 eV kinetic energy, has a mean free path of 8.76 Å in a Mn host material, 6.49 Å in a Ni host, and 11.65 Å in a Sb host. The Mn photoelectrons mean free path used in the above sums is the average value of $\lambda_{\mathrm{avg}}^{\mathrm{Mn}} = 9.48$ Å.

Table 4. Approximation of the theoretical escape depths for the Mn, Ni and Sb, obtained by taking the average of the respective impurity mean free paths in different pure host materials.

Element	E_{kin} (eV)	a	b	λ in Mn (Å)	λ in Ni (Å)	λ in Sb (Å)	λ_{avg} (Å)
Mn	613	19.7	−2.87	8.76	8.05	11.65	**9.48**
Ni	399.5	23.7	−3.21	6.49	6.06	8.45	**6.99**
Sb	716	12.4	−2.18	9.81	8.99	13.15	**10.65**

As mentioned above, the lifetime of an ordered stoichiometric NiMnSb surface, at room temperature, is only approximately several hours, even in ultrahigh vacuum conditions. After performing the same cleaning procedure for three similar samples, we have observed that continuing the thermal treatments at 400 °C for more than several minutes resulted in activation of surface segregation. LEED images showed that the segregated surface remained ordered, with the same lattice constant of 6 Å. Only after the analysis of the angle resolved XPS intensity ratios, shown in figure 20, revealed a substantial deviation from the perfect bulk termination surface stoichiometry, which is expected from other studies as well [31].

Qualitatively, figure 20 shows that both Mn/Sb and Mn/Ni intensity ratios bend upward with increasing emission angle and annealing time, whilst the Ni/Sb ratio is not only very small compared with the other two, but also almost constant as a function of emission angle. This result can be explained only if the surface region (high emission angles) is Mn rich and so, the proportionality of the three elements is altered as we probe closer to the surface terminal layer.

In order to analyse the Mn surface segregation phenomenon quantitatively, we again used the fitting procedure introduced above. The measured XPS ratios are fitted with a model in which the Mn atoms can segregate to both vacancy sites as well as replace both Sb and Ni atoms. The Mn atomic fraction in the surface region can be written as:

$$f_j(\text{Mn}) = b + \delta \exp\left(-\frac{jd}{G}\right) \tag{8}$$

where b is the bulk atomic fraction of 0.5 for the Mn/Sb layers ($j = $ even) and $b = 0$ for the Ni/vacancies planes. The contribution to the intensity peaks for each elemental core can be summed for the corresponding layer, as follows:

$$
\begin{aligned}
I(\text{Mn}) &= \sum_{j=0}^{\infty} 0.5 \exp\left(-\frac{2j}{\lambda_{\text{Mn}} \cos\theta}\right) + \sum_{j=0}^{\infty} \delta \exp\left(-\frac{j}{G} - \frac{j}{\lambda_{\text{Mn}} \cos\theta}\right) \\
&= \frac{0.5}{1 - \exp\left(-\frac{2}{\lambda_{\text{Mn}} \cos\theta}\right)} + \frac{\delta}{1 - \exp\left(-\frac{1}{G} - \frac{1}{\lambda_{\text{Mn}} \cos\theta}\right)} \\
I(\text{Ni}) &= \sum_{j=0}^{\infty} 0.5 \exp\left(-\frac{2j+1}{\lambda_{\text{Ni}} \cos\theta}\right) - \sum_{j=0}^{\infty} \delta \exp\left(-\frac{2j+1}{G} - \frac{2j+1}{\lambda_{\text{Ni}} \cos\theta}\right) \\
&= \frac{0.5 \exp\left(-\frac{1}{\lambda_{\text{Ni}} \cos\theta}\right)}{1 - \exp\left(-\frac{2}{\lambda_{\text{Ni}} \cos\theta}\right)} - \frac{\delta \exp\left(-\frac{1}{G} - \frac{1}{\lambda_{\text{Ni}} \cos\theta}\right)}{1 - \exp\left(-\frac{2}{G} - \frac{2}{\lambda_{\text{Ni}} \cos\theta}\right)} \\
I(\text{Sb}) &= \sum_{j=0}^{\infty} 0.5 \exp\left(-\frac{2j}{\lambda_{\text{Sb}} \cos\theta}\right) - \sum_{j=0}^{\infty} \delta \exp\left(-\frac{2j}{G} - \frac{2j}{\lambda_{\text{Sb}} \cos\theta}\right) \\
&= \frac{0.5}{1 - \exp\left(-\frac{2}{\lambda_{\text{Sb}} \cos\theta}\right)} - \frac{\delta}{1 - \exp\left(-\frac{2}{G} - \frac{2}{\lambda_{\text{Sb}} \cos\theta}\right)}
\end{aligned}
\tag{9}
$$

where the λs are the corresponding mean free paths given in table 4, and the characteristic segregation parameters δ and G were considered fitting parameters. The fitting procedure was:
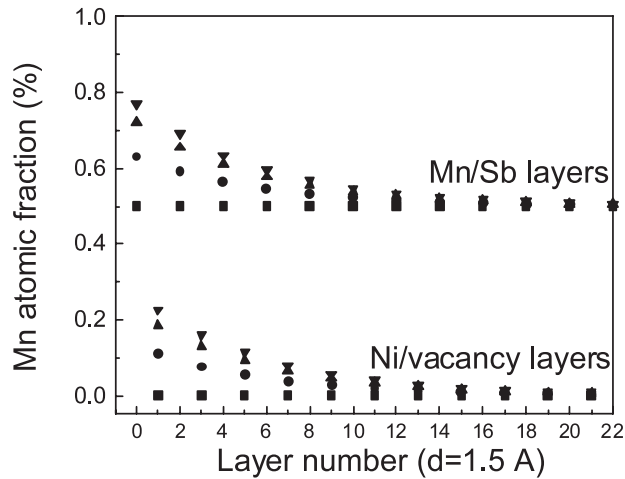
Figure 21. The Mn concentration in the near surface region obtained from fits of the angle dependent XPS ratios. The symbols are identical to the ones used in figure 20. Adapted from [48].

Table 5. The fitting parameters used for modelling the experimental ratios in figure 20. δ represents the segregation at the surface–vacuum interface and G is the segregation depth, expressed both in Å and in units of distance ($d = 1.5$ Å) between layers.

Annealing time	G ($d = 1.5$ Å)	G (Å)	δ (%)
5 min at 400 °C	5.7	8.55	13
15 min at 400 °C	5.7	8.55	22
30 min at 400 °C	5.7	8.55	27

(1) assume a certain stacking sequence, (2) fit the Mn/Ni experimental ratio by adjusting δ and G, (3) calculate the Mn/Sb ratio given the fit to the Mn/Ni ratio, and (4) if the calculated ratios of the previous steps do not fit the corresponding experimental ones, then try a new stacking sequence. The best results of the fitting procedure for three different surfaces are shown as continuous lines in figure 20, together with stoichiometric surface (assumed to be segregation free). The fitting parameters used in the models are presented in table 5.

The surface concentration profiles were easily constructed using equation (8) and the values of δ and G obtained above. Figure 21 presents the Mn concentration dependence upon layer number for the three heavily annealed surfaces. Note that the same figure also contains the constant Mn atomic fraction of 0.5 for the Mn/Sb layers and 0 for the Ni/vacancy layers, characteristic of a stoichiometric structure for the freshly prepared surface. This surface termination of MnSb, for the stoichiometric surface is entirely consistent with the predictions of Jenkins and co-workers [38, 43, 75, 76] and others [42, 44].

When equilibrium is established between the surface and the bulk, the surface enthalpy is quite different from the bulk [65]. Surface segregation is a strong indication that the surface enthalpy differs significantly from the bulk, in the context of standard statistical models. In a simple statistical mechanical model of segregation [83], the total free energy, F, for the system is written as:

$$F = \sum_i n_i^{\mathrm{b}} g_i^{\mathrm{b}} + n_i^{\mathrm{s}} g_i^{\mathrm{s}} - k_{\mathrm{B}} T \ln \Omega, \qquad (10)$$

where n_i^{b} and n_i^{s} are the number of the bulk and surface atoms of type i, with individual free
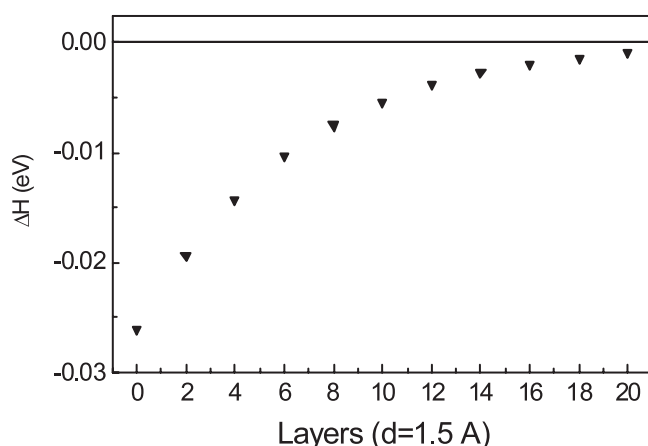
Figure 22. The enthalpy difference between the surface and the bulk based on the most extensive Mn segregation shown in Figure 21 (down-triangles). Adapted from [48].

energies g_i^s and g_i^s, respectively; k_B is the Boltzmann constant, T is the temperature of the system, and Ω is the entropy due to the mixing of the components. For a two-component system, an Arrhenius expression can be written as:

$$\frac{n_A^s}{n_B^s} = \frac{n_A^b}{n_B^b} \exp\left(-\frac{H}{k_B T}\right), \tag{11}$$

where H is the enthalpy of the segregation. Equation (13) implies that the surface segregation is a competition to minimize the total free energy by a maximization of entropy by evenly mixing the two elements. Using the bulk concentration values for the A and B components, one can easily extract the dependence of the segregation enthalpy of the atomic fraction.

We can calculate the dependence of enthalpy as a function of layer number, as demonstrated in figure 22, for the most extensively Mn segregated surface (after 30 min annealing at 400 °C). This difference in enthalpy can be related to the creation of a surface electronic structure very different from the bulk (i.e. surface states for the stoichiometric surface), can result in a new surface lattice structure distinct from the bulk and, of course, can become the driving force for segregation. This energy difference, between the surface and the bulk, appears to be more than sufficient to overcome the energy barriers to defect formation, that have been thought to hinder defect mediated reduction in polarization [84, 85]. In addition, defects and variations in the local lattice order are believed to strongly influence the net electron polarization near the Fermi level, as discussed in the next section.

5. Surface and bulk Debye temperatures

The thermal motion of the surface atoms dictates many of the physical and chemical properties such as: surface diffusion [86, 87]; anharmonicity leading to roughening transitions [88–90]; surface reconstructions [91, 92]; which all influence the extent of compositional inhomogeneities, including defects. The key descriptive parameter of the dynamic motions of atoms on the surface, as well as in the bulk, is the Debye temperature.

We investigated the effective surface Debye temperature of the NiMnSb(100) using photoemission (XPS) and low energy electron diffraction (LEED) techniques which we compared to the bulk Debye temperature calculated from the phonon dispersion curves obtained

from inelastic neutron scattering [93]. This comparison is one of a very limited number of such studies in complex compound materials [94, 95] and the first for the Heusler alloys.

The dynamic motions normal to the film surface dominate the surface Debye temperature θ_D determined by most electron spectroscopy techniques using the Debye–Waller model [96, 97]. This surface θ_D is dominated by the atoms' dynamic motions parallel to the scattering vector and typically does not contain significant in-plane or anharmonic contributions to the true surface Debye temperature. We regard this parameter (θ_D) as the measure of the dynamic motions of specific atoms along the direction of the surface normal. For LEED spot with intensity I, we used the formula:

$$I - I_0 \exp[-2W(T)], \tag{12}$$

where $W(T)$ is the Debye–Waller factor. W is given by:

$$2W(T) = |\Delta k|^2 \langle u_0 \rangle^2, \tag{13}$$

in which Δk is the wavevector transfer and $\langle u_0 \rangle^2$ is the mean squared displacement of the atoms. In the framework of Debye theory, the factor W can be approximated in the first order as [96, 98]:

$$2W = \frac{3\hbar^2(\Delta k)^2 T}{m k_B \theta_D^2}, \tag{14}$$

where W is the Debye–Waller factor, $\hbar$ is Planck constant, T is the sample temperature, $\hbar(\Delta k)$ is the electron momentum transfer, m is the mass of the of the scattering centre, k_B is the Boltzmann constant, and θ_D is the effective surface Debye temperature.

The scattering vector is obtained from equation:

$$\Delta k = 2k \cos \frac{\theta}{2} = \frac{4\pi}{\lambda} \cos \frac{\theta}{2}, \tag{15}$$

where θ is the angle between the incoming and outgoing electron beams and λ is the wavelength of the electrons. The mass of the scattering centre is approximated by an average value of the three different atomic masses contained in a unit cell:

$$m = [M_{Mn} + M_{Ni} + M_{Sb}]/3 = 78.45 \text{ au}. \tag{16}$$

Figure 23 shows the temperature dependence of the intensities from backscattered low energy electron diffraction, after background subtraction (I_{bk}) and normalization to the value (I_0) at the lowest temperature. The three sets of data shown were taken using different incident electron energies of 33, 58 and 83 eV. The angle θ from equation (15) varied very little in our experiment and the change in scattering vector (Δk) largely comes from the different electron energies employed. The change in LEED intensities, plotted in figure 23 as the slope of $\ln[(I - I_{bk})/I_0]$, increased with increasing (Δk) or with increasing incident (and backscattered) electron energies. Using equation (14), the values obtained for the effective surface Debye temperature are 140 ± 20 K (at 33 eV incident electron energy), 143 ± 20 K (at 58 eV) and 154 ± 20 K (at 83 eV). The electron's mean free path increases and so does the probing depth with increasing incident (and backscattered) electron energies. We consider that the effective Debye temperature obtained at the lowest electron energies is the most representative of the dynamic normal atomic motions in the thin film surface region. The other two values, at higher electron energies, include the normal vibrations of the atoms situated increasingly deeper in the selvedge (near surface) region.

In the case of photoemission spectroscopy (XPS), the most common geometry used is the one in which the outgoing electrons are emitted in the normal direction ($\theta = 0$). In this case the momentum transfer is equal to the momentum of the emitted electron: $\Delta k = 2\pi/\lambda$. In
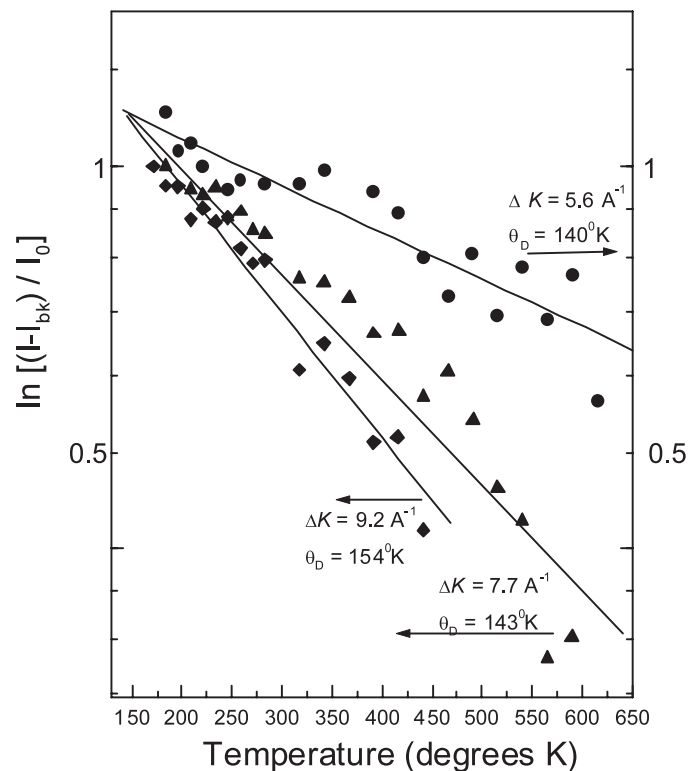
Figure 23. Logarithm of the intensities of the diffracted electron spots obtained in LEED, after background subtraction (I_{bk}) and normalization to the value (I_0) at the lowest temperature. The three sets of data were obtained using different incident electron energies: 33 eV (circles), 58 eV (up-triangles) and 83 eV (diamonds). The direction of the incident electrons was along the surface normal. Adapted from [93].

our experiments, we monitored the photoelectron intensity from the 3d shell of the Sb atoms using Mg Kα radiation (1253.6 eV, with a FWHM of 0.65 eV), and appropriately corrected for the scattering centre mass. The temperature dependence of the $3d_{3/2}$ core level of antimony, obtained from x-ray core level photoemission, is shown in figure 24. This particular core level has a narrow and intense line shape at all temperatures. The temperature dependence of the Sb $3d_{3/2}$ core level peak intensities is shown in the right panel of figure 24 and using equations (12) and (14) we obtain a value of 144 ± 10 K for the effective surface Debye temperature. The mean free path of the ejected electrons in normal emission is no more than 20 Å from the free surface and so the sample probing depth is limited to the surface and selvedge region.

For comparison with the above values, we extracted the Debye temperature for bulk single crystals from the wavevector dependent inelastic neutron scattering (a bulk sensitive technique) [90]. Neutron inelastic scattering is a common technique for mapping the dispersion curves for acoustic and optical phonons, as well as the magnon dispersion. For values of the scattering vector q close to zero, the dispersion of the acoustic oscillatory modes is linear, and the slope of this linear dependence is related to specific elastic constants, depending on the scanning direction.

The bulk Debye temperature of single crystals can be estimated from application of the Debye model and the phonon dispersion curves [99]. In this model, the upper limit ν_D to the
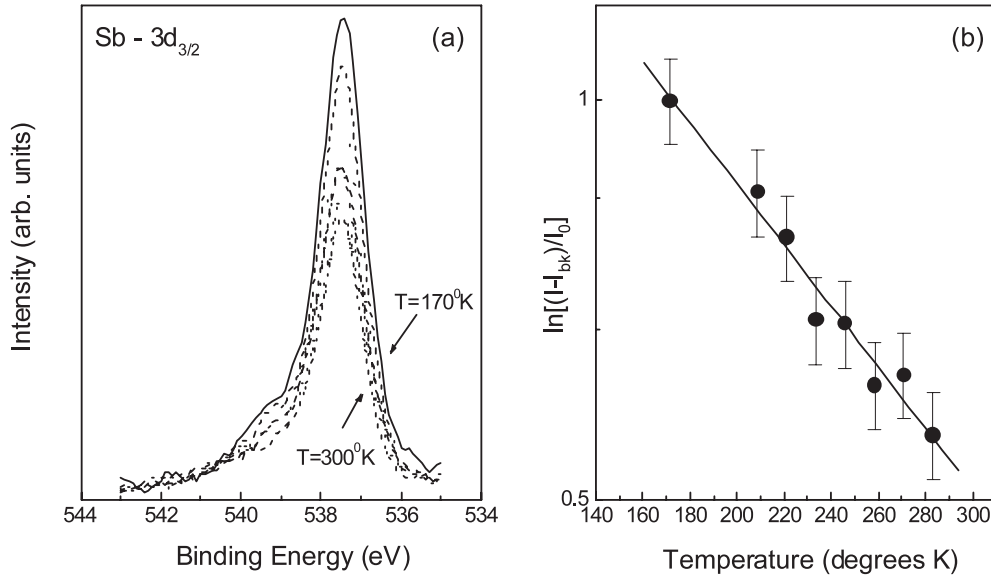
Figure 24. (a) Normal x-ray photoemission spectra of Sb $3d_{3/2}$ core level for various temperatures after background subtraction. (b) Logarithm of the intensity I of the Sb $3d_{3/2}$ core level versus temperature after background (I_{bk}) subtraction and normalization to the value I_0 at the lowest temperature. Adapted from [93].

frequency is obtained from the normalizing condition that the total number of oscillatory modes is equal to $3r N_A$ per mole, where r is the number of atoms per unit cell (and N_A is Avogadro's number). The quantity ν_D is related to the parameter θ_D by:

$$\nu_D = \frac{k_B}{h}\theta_D. \tag{17}$$

Thus, the frequency limit ν_D and the related parameter θ_D, the Debye temperature, can be obtained from the formula [100]:

$$\frac{4\pi V}{3}(c_L^{-3} + 2c_T^{-3})\nu_D^3 = 3r N_A, \tag{18}$$

in which V is the molar volume and c_L, c_T are the corresponding longitudinal and transverse wave velocities. For cubic crystals, the velocities are related to the elastic constants C_{11} and C_{44} as follows [100]:

$$
\begin{aligned}
c_L &= \sqrt{\frac{C_{11}}{\rho}} \\
c_T &= \sqrt{\frac{C_{44}}{\rho}},
\end{aligned}
\tag{19}
$$

where $\rho = 7610$ kg m^{-3} is the mass density. (Note that the elastic constants 'C' have the dimensions of [energy]/[volume] [100].)

The inelastic neutron scattering experiments [101] were carried out at the Institute Laue-Langevin, using the IN1 (hot neutrons) and IN8 (thermal neutrons) spectrometers, in order to cover all transfer energies values from 0 to 120 meV. The measurements were made on three single crystals, with sizes ranging from 100 to 2000 mm^3 whose mosaic spread was
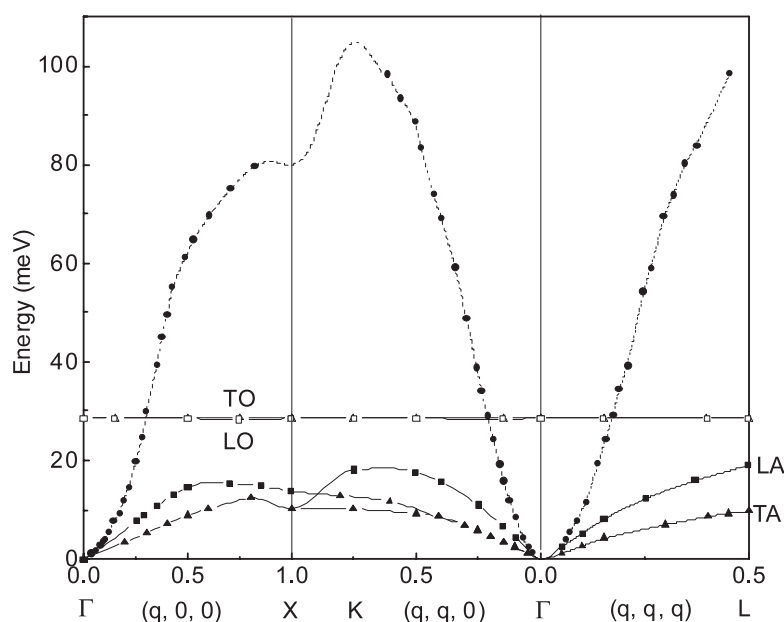
Figure 25. Dispersion curves for magnons (circles), longitudinal phonons (squares), and transverse phonons (up-triangles) at 300 K obtained in neutron scattering. No magnetic field was applied. Adapted from [93, 101].

less than 0.5°. Excitations were investigated mainly at room temperature in the direction of the high symmetry axis (100), (110) and (111). No magnetic field was applied. Constant energy scans were generally performed to investigate the magnon dispersion, whereas constant-q scans were used to locate and map the wavevector dependence of the acoustic and optical phonons. Figure 25 presents the complete experimental phonons and magnons dispersion curves at 300 K [51, 93, 101].

For a material with three atoms in the primitive cell, we generally expect three acoustic and six optical branches, whereas only one (twofold-degenerate) branch of magnons was observed. Longitudinal acoustic phonons reach a maximum energy for q close to (0.6, 0, 0) in the $\langle 100 \rangle$ direction and (0.7, 0.7, 0) in the $\langle 110 \rangle$ direction. One very flat optical branch was observed at energy of about 29 meV, with little difference in energy for longitudinal and transverse directions. (One explanation for this dispersionless optical mode is the arrangement of the Ni atoms in the cubic structure. Among the closest neighbour lattice sites to nickel are the vacancy sites.)

The elastic constants can be easily extracted from the slope of the acoustic modes in each Γ point, depending on the scanning direction. For the $\langle 100 \rangle$ longitudinal mode, $C_{11} = 138$ GPa, for the $\langle 110 \rangle$ transverse mode 1, $C_{44} = 45$ GPa and for the $\langle 110 \rangle$ transverse mode 2, $C_{12} = 48$ GPa [93, 101]. Using these values to calculate the longitudinal and transverse mode velocities in the equation (21), we obtained a value of the bulk Debye temperature of 312 ± 5 K [93].

Almost independently of surface orientation we would expect that the effective surface Debye temperature is of the order of 70% (i.e. $1/\sqrt{2}$) of the bulk value of the Debye temperature [96–98]. This is due to the fact that the surface atoms have only half of the number of nearest neighbours that surround the bulk atoms [96]. Comparing the values of the Debye temperature obtained for the NiMnSb(100) Heusler alloy, the surface temperature is almost

26

45% of the bulk value. This drop in the Debye temperature between the surface and the bulk is not unexpected, under our preparation conditions, if we take into account that the surface and selvedge regions have different compositions from the bulk [32, 48]. Indeed, as shown in [48], manganese segregation occurs at the NiMnSb(100) surface and, in the surface region, the vacancies in the nickel plane(s) are filled with Mn while the Ni to Sb ratio remains relatively unperturbed. In addition, there are several other phenomena that may contribute to the lowering of the surface Debye temperature with respect to the bulk. The motion of the surface atoms is not isotropic, the force constants at the surface can be appreciably different from those in the bulk, and, in general, the surface may contain anharmonic phonon modes that differ from the bulk [102, 103].

The reduced surface Debye temperature will lower the barriers to surface segregation and can be a consequence of the compositional differences due to segregation. The polarization asymmetry representative of the vacuum–alloy interface could be strongly influenced by the thermal oscillations of the atoms in the surface region [41].

6. Characterization of the surface electronic structure

The understanding of the electronic structure is the key to gathering insight into many characteristics of a solid, including the dielectric, magnetic and bonding properties. Fundamental issues related to magnetism, such as the exchange coupling, the spin–orbit coupling, the magnetic moment, and the Curie temperature are determined by the electronic structure. The valence and conduction band structure can be experimentally investigated with photoemission, inverse photoemission and x-ray absorption.

Using the surface preparation technique described in section 4, we were able to characterize an epitaxial and stoichiometric surface of NiMnSb. Establishing the correct stoichiometric surface composition of the NiMnSb(100) surface, determined with both LEED and XPS as demonstrated in section 4, was essential for the spin polarized IPES, which is a highly surface sensitive technique. The choice of spin polarized inverse photoemission for determining polarization is dictated by several considerations. Spin polarized inverse photoemission can be more readily compared to magnetic circular dichroism and spin polarized appearance potential spectroscopy as all three probe the unoccupied band structure [104], while spin polarized photoemission does not. Furthermore, depolarization due to the ground state non-quasiparticle density of state should be most significant in the unoccupied density of states just above the Fermi level for NiMnSb [61].

The NiMnSb sample was installed in a UHV system, inside a coil which is used to switch the in-plane magnetization direction. A pulsed 400 Oe magnetic field was applied along the ⟨110⟩ easy magnetization direction, representing a far larger value than the sample's saturation and coercive fields of 40 and 32 Oe, respectively. The spin up and down densities of states near the Fermi level for a stoichiometric surface (figure 26) were measured at room temperature and normal incidence of the incoming electron beam. The polarization at the Fermi level is as high as $67 \pm 9\%$, or nearly 100% above background, as shown in the lower panel of figure 26. Note that the spin asymmetry shown in figure 26 is calculated as a function of incident electron energy using equation:

$$P = \frac{N_\uparrow - N_\downarrow}{N_\uparrow + N_\downarrow}, \tag{20}$$

where $N_\uparrow$ and $N_\downarrow$ are the spin up (down) density of states, respectively. This asymmetry value measured in spin polarized IPES is significantly higher than the polarization asymmetry of 50%, at room temperature, measured from a polycrystalline sample using spin polarized
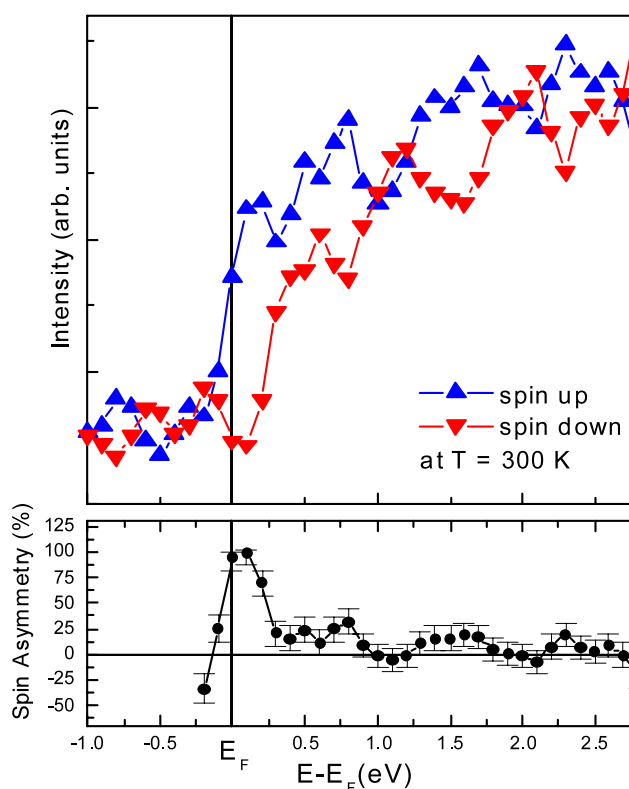
Figure 26. Spin polarized unoccupied electronic bands from spin polarized inverse photoemission spectroscopy at normal incidence for the stoichiometric NiMnSb surface, at 300 K. The bottom panel shows the corresponding spin asymmetry near E_F. Adapted from [32].

photoemission [26], even when the background is included, and much higher that the spin polarized inverse photoemission data obtained by Grenz [30]. For these previously reported spin polarized photoemission measurements, Sb segregation was observed, which would tend to lower the polarization. The data taken at 300 K from the stoichiometrically ordered alloy surface indicate a conduction band edge, in spin minority, at about 250 meV above the Fermi level. The high values of polarization near the Fermi level in our spin polarized inverse photoemission data at room temperature do suggest that depolarization (a reduction of polarization from 100%), due to the ground state non-quasiparticle density of states [61, 62], is quite small.

According to calculations for NiMnSb [2], the Fermi level intersects the centre of the gap (or slightly above centre), in spin minority. Thus, these spin polarized data (at the surface Brillouin zone centre or $k_\parallel = 0$) are consistent with both a calculated gap in spin minority of about 0.5 eV and a half-metallic system. The data may not, however, be considered as conclusive proof that NiMnSb is indeed a half-metallic system. Such a definitive statement would require mapping the electronic densities of states in more than one k space points across the Brillouin zone, particularly in the vicinity of the spin majority Fermi level crossings as well as ensuring that the polarization is not a result of surface states. The short 'lifetime' of the clean, stoichiometric surfaces (of the order of 4–5 h) made it impossible to perform the required studies needed to prove the half-metallic character across the entire Brillouin
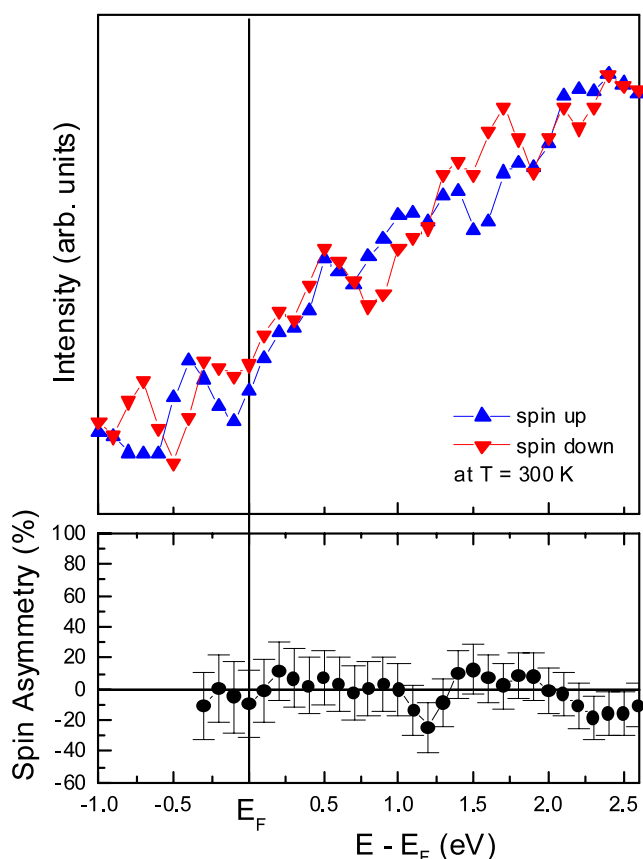
Figure 27. Spin polarized unoccupied electronic bands from spin polarized inverse photoemission spectroscopy at normal incidence for the Mn rich NiMnSb surface, at 300 K. The bottom panel shows the corresponding spin asymmetry near E_F. Adapted from [32].

zone, as the final spectrum must be obtained by summing experiments from several samples stoichiometric surface. Sputtering and annealing of NiMnSb ordered surfaces (performed to ensure contamination free surfaces) leads to a degradation of surface composition, including Mn segregation, as presented in section 4, and such data cannot be used. What experimental band mappings that do now exist have been taken using photoemission (where the data collection is faster) are spin integrated [105].

The influence of the Mn segregation on the unoccupied band structure of NiMnSb results in a drop of the polarization asymmetry and a loss of density of states near the Fermi level, as can be observed in figure 27. These changes in polarization and density of states represent a decrease in surface metallicity along with the disappearance of the inferred gap in the spin minority subband and, therefore, loss of half-metallic character in the surface [11, 49, 50]. The behaviour of this segregated surface is more reminiscent of a MnSb binary alloy [106–109] or of an antiferromagnetically aligned Mn rich surface layer, than of the expected electronic structure of NiMnSb.

The unoccupied bands above the Fermi level obtained from IPES, can be assigned to each atomic constituent in the sample by comparing the IPES and XAS spectra [104]. The sample used in the XAS study was capped with 25 Å of Al for protection against oxidation as is well
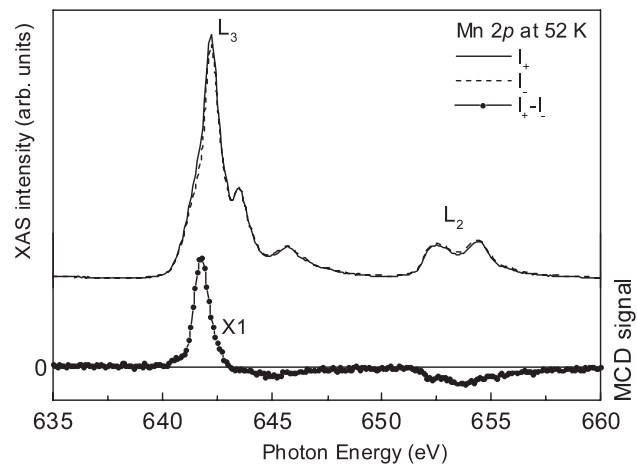
Figure 28. Absorption spectra for L_3 and L_2 edges of Mn at 52 K. The lower curve shows the corresponding MCD signal obtained as the difference between XAS signals with opposite magnetization directions. Adapted from [33].

known to have a very small cross section for the energies involved in this technique. Given that the total Al thickness was too small to affect significantly the probing depth of the absorption spectra, we assume that Al does not alter the NiMnSb surface composition and, therefore, the XAS spectra must be compared to the IPES spectra measured on a clean, stoichiometric surface, free of Mn segregation.

The XAS and XMCD spectra were measured at the U4B beamline located at the National Synchrotron Light Source (NSLS) at Brookhaven National Laboratory. The XAS spectra were measured by total electron yield detection (TEY) in 45° sample orientation with respect to the incoming beam, in vacuum less than 5×10^{-10} Torr. We recorded two total electron yield spectra, one with the incident light helicity (circular polarization) oriented parallel to the remanent magnetization of the sample, and one antiparallel. The XAS spectrum is the average of these two spectra, while the XMCD is the difference between the two. For the measurements included in this work, the light helicity was kept constant while the remanent magnetization of the sample was reversed by reversing a magnetic field applied parallel to the sample. The spectra were normalized to the incident flux via the current measured through a gold mesh that was placed in the beam in front of the sample.

In accordance with the corresponding selection rules detailed in [104], we have measured the absorption edge induced by the transition from the 2p initial state to the 3d final state, for both Mn and Ni ferromagnetically aligned sublattices. The XAS and MCD spectra obtained for the Mn L_2 and L_3 edges at 50 K are shown in figure 28. The spin–orbit splitting for the Mn atoms is given by the energy difference between the L_2 and L_3 peaks, approximately 11.5 eV. This value is very close to the spin–orbit coupling found in the Mn single crystal. The direct effect of the crystalline lattice on Mn atoms can be observed in the fine structure of both edges. The L_3 peak is split in three, while the L_2 edge is a doublet. The calculations found in [110] correspond well with our data in the case of cubic symmetry of the crystalline Mn lattice, which also represents the symmetry of the half-Heusler alloy. The splitting introduced by the crystal field is stronger than any multiplet effects (2p–3d hybridization), which are shown to influence the L edge of any transitional metal [111]. The Mn MCD signal, shown in the lower part of each panel in figure 28, is positive in the L_3 edge and negative for the L_2 edge.
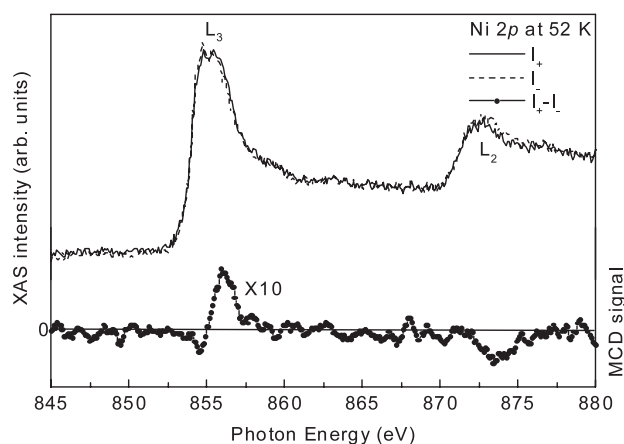
Figure 29. Absorption spectra for L_3 and L_2 edges of Ni at 52 K. The lower curve shows the corresponding MCD signal obtained as the difference between XAS signals with opposite magnetization directions. The MCD intensity scale is reduced by a factor of 10 compared to the MCD intensity scale of Mn in figure 28. Adapted from [33].

The corresponding Ni XAS and MCD spectra are presented in figure 29 at a temperature of 52 K. The spin–orbit coupling strength is 16.8 eV—the same as in a Ni single crystal. The fine structure of the Ni absorption peaks is not very pronounced, consistent with a $3d^9$ initial state [110]. The crystal field has no influence on the shape of the L edge corresponding to an almost full 3d band metal [111]. The Ni dichroic signal remains positive (negative) for the L_3 (L_2) edge as in the case of Mn, indicating a ferromagnetic coupling between Mn and Ni. Note that the intensity of the Ni dichroic signal is ten times less than the Mn dichroic signal, as shown in the figure 29. This drop of the dichroic intensity is in agreement with the experimental values obtained for the local moments using polarized neutron diffraction [33, 59]. The Sb 3d XAS spectrum (not shown here) is dominated mainly by the oxygen peak from the Al cap layer, which interferes with the 3d spin–orbit coupling. The presence of oxygen (for the oxidation of the aluminium capping layer) introduces great difficulties in interpreting the shape of the Sb XAS spectrum but this should not affect the MCD signal. The local magnetic moment of Sb, given by the total area of the MCD signal, is negligible—of the order of 0.1 μ_B and in agreement with band calculations [31].

The comparison between spin polarized inverse spectrum of the unoccupied density of states and x-ray absorption spectra (XAS) for Mn 2p and for Ni 2p can be made, due to the fact that both techniques generally probe the same final states, as noted above [104]. Figure 30 shows the comparison of the SPIPES and XAS spectra for NiMnSb(100) at room temperature. For both MCD and XAS spectra, the conduction band edge (the approximate Fermi energy) for the XAS spectra is assigned on the basis of the experimentally measured core level binding energies for NiMnSb(100): 640.2 eV for the Mn $2p_{3/2}$ and 853.3 eV for the Ni $2p_{3/2}$ (figure 20). In the XAS spectra, the unoccupied states are shifted to slightly higher energies above E_F than in SPIPES, as expected from the perturbation of the Coulomb interaction with the photoexcited core–hole. Nonetheless, from this comparison, we can establish a rough correspondence of the unoccupied states in inverse photoemission. The density of states just above E_F, at approximately 0.63 eV, is largely Mn in origin (figure 30), as derived from our XAS/MCD studies, and this is generally consistent with other XAS/MCD studies [112, 113], and recent spin polarized appearance spectroscopy measurements [31]. Our Mn XAS spectra
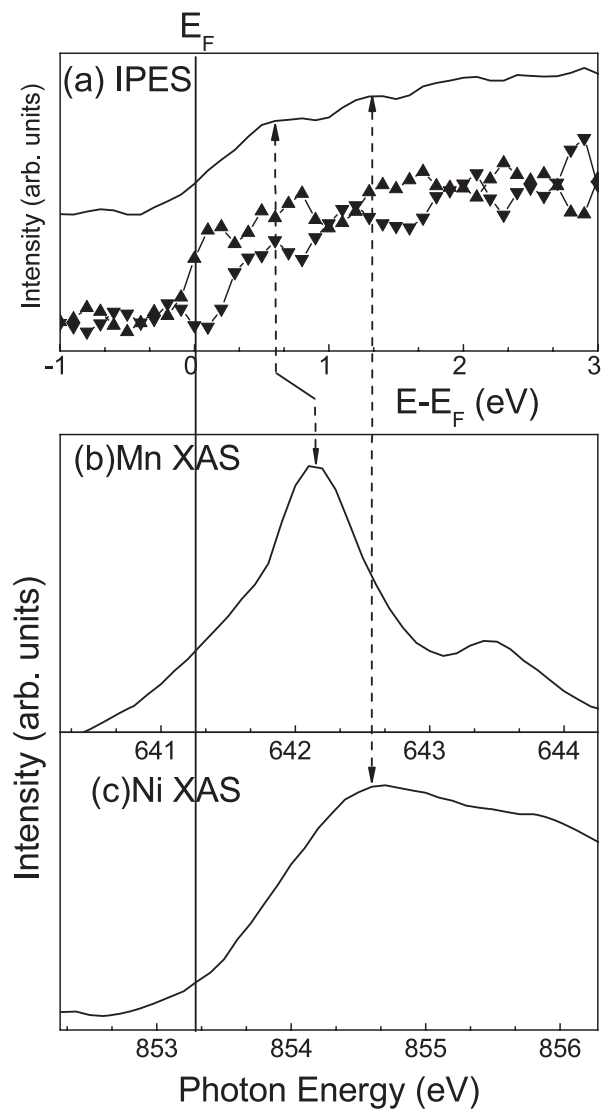
Figure 30. The comparison of the SPIPES, MCD and XAS spectra for NiMnSb(100). The spin polarized inverse photoemission (SPIPES) (▲: spin up, ▼: spin down) and integrated (continuous line) data for the stoichiometric NiMnSb(100) clean surface at 300 K (a) are compared x-ray absorption results of Mn 2p (b) and Ni 2p (c) core–hole spectra. Adapted from [33].

are characteristic of a Mn d^5 initial state (and could include the expected d^4 contributions) [113] at all temperatures from 45 to 250 K. The Ni d^9 initial state contribution to the joint density of unoccupied states measured in IPES is further away from the Fermi level, at approximately 1.3 eV.

It is now clear that NiMnSb(100) does have surface states. Theoretically, these surface states are spin minority, and cross the Fermi level away from $\overline{\Gamma}$ [9, 38, 42–46, 105]. Indeed there is now experimental confirmation of at least some surface states at the surface of NiMnSb(100) [105].
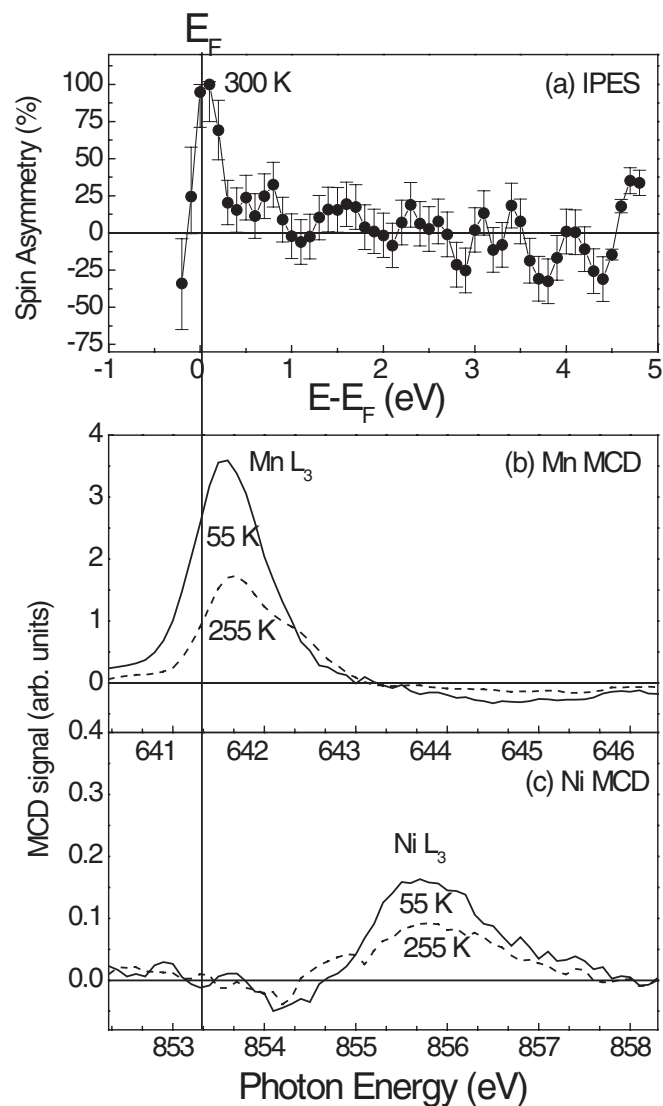
Figure 31. The spin asymmetry obtained in SPIPES at 300 K is compared with MCD signal across both the L$_2$ and L$_3$ edges of Mn (b) and Ni (c) at 55 K and 255 K. Adapted from [33].

7. Evidence for temperature dependent magnetic moment ordering in NiMnSb films

The polarization of the clean NiMnSb(100) surface is determined by the difference of spin up and down in spin polarized IPES (figure 26). These results are compared with the MCD signal, which is obtained as the difference between XAS signals with opposite magnetization directions, as indicated in figure 31. The large polarization asymmetry and the strong contribution from the Mn spin and orbital moments, at remanence, are apparent in the region close to the Fermi level (nearly 100% above background for $k_\parallel = 0$).

Since polarization at the Brillouin zone centre ($k_\parallel = 0$) does correspond to long range magnetic order, it is not clear whether the polarization may, in fact, be easily related to the

magnetic moment for any given system. Just above the Fermi level, spin polarized inverse photoemission measurements provide a polarization close to 100% at 300 K, in Brillouin zone centre ($k_{\parallel} = 0$) (figure 31(a)). As the temperature is decreased below 80 K, the MCD exhibits a huge increase in relative spin and orbital moment, as shown in figure 31(b) and (c). Yet in XAS, the apparent density of states near the Fermi level (threshold) does not change significantly for either Mn or Ni. Therefore, the fact the polarization of NiMnSb(100) is close to 100% at an elevated finite temperature (300 K here) at the Brillouin zone centre ($k_{\parallel} = 0$) is not a good indicator of the maximum possible remanent band moment or, indeed, of the total 'integrated' band polarization in the NiMnSb system, as was noted previously.

Because magnetic circular dichroism is sensitive to band structure polarization (dependent upon symmetry and wavevector), to the remanent unoccupied band polarization, to the magnetocrystalline anisotropy (the crystal field) [114, 115], to the excitation cross sections (particularly in non-transmission absorption geometries) and to an often undetermined surface contribution, MCD does not accurately probe the saturated local moment of the bulk material. More accurate measurement of the local bulk sample moment can be obtained from neutron scattering (although this is a less sensitive measure of the global moment that includes local fluctuations). The Fourier transform of the magnetic scattering factor, from neutron scattering, again demonstrates that most of the moment is localized on the Mn sites [59]. The total moment from high field magnetometry (at 10 K) is 4.025 μ_B per formulae unit, consistent with half-metallic character (we attribute the possible excess moment to altered stoichiometry and/or polarization of the inner shells). From polarized neutron scattering we find the local moment on the Mn at 15 K, 3.79 ± 0.02 μ_B, falls to 3.55 ± 0.02 μ_B at 260 K, while the local moment on the Ni sites change little, with values varying around 0.18 ± 0.02 μ_B, so that the total unit cell moment is some 3.98 ± 0.03 μ_B/atom [48], as noted previously. The fact that the local moments changes, even under high field conditions, suggests that there is a change in the moment coupling between Mn and Ni at a temperature of about 80 K, as is now also suggested by theory [41]. At higher temperatures, above 80 to 100 K, the saturation moment is lower than that expected for a half-metallic ferromagnet.

The temperature dependence of the local magnetic moments of Mn and Ni were obtained by integrating the MCD signals across both the L_3 and L_2 edge, or only across the L_3 edge, at each temperature. As shown in figure 32, the MCD data provide clear evidence of an increased moment ordering in the case of Mn, with its persistent strong local moment. The moment increase is also observed below 80 K in the case of Ni, and is accentuated if the MCD signals are integrated across both $L_3 + L_2$ edges.

The observed increase in the local moment, on the Mn in neutron scattering, and on the Mn and Ni atoms in NiMnSb below 80–100 K in MCD (figures 32 and 33(a) and (b)) are consistent with the increase in the change in ($\Delta\rho/\rho$) magnetoresistance below 80 K (shown in figures 14 and 33(d)), and the increase in the $\langle 200 \rangle$ neutron magnetic scattering factor, as indicated in figure 15. As noted previously, the resistance of NiMnSb with temperature fits a $T^{1.65}$ power law above 80 K (close to $T^{3/2}$), but follows a T^2 power law below 80 K, as shown in figures 12 and 33(c). The temperature dependence of the resistivity is therefore also consistent with a crossover in magnetic ordering at 80–100 K, though the material remains ferromagnetic. Fitting the MCD L_3 edge data in figure 32 to an Arrhenius expression (consistent with moment fluctuations), indicates that the critical temperature for the classical ferromagnetic to half-metallic ferromagnetic (moment ordering) phase transition is between 80 and 100 K.

The changes in the magnetic structure factor(s), shown in figure 15, suggest a loss in the strong local moment ordering and/or alignment between Ni and Mn. The change in structure factor suggests a subtle rearrangement of the magnetization density between Ni and Mn. The transfer of only a small amount of electron density, say just a few hundredths of
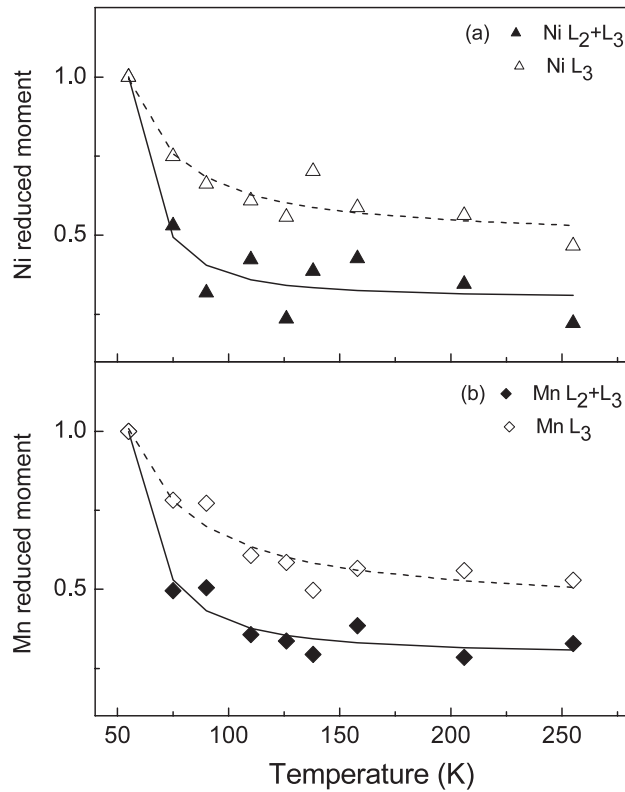
34

Figure 32. The relative Ni (a) and Mn (b) local moment derived from MCD. The relative moment, obtained by normalization with the value at lowest temperature, contains both spin and orbital contributions from the L_3 edge (open symbols) and the sum of both the L_3 and L_2 edges (filled symbols). Adapted from [33].

an electron to the down spin subband or from Mn to Ni, may not result in much change in either the total moment or the Mn saturation moment (say by about 0.05 μ_B), but could substantially change the net band polarization near the Fermi level [41]. This effect tends to appear as though there is a failure to completely saturate the magnetization in the MCD measurements, taken at remanence, with increasing temperature. The large change in the MCD signal derived moment compared to the smaller change in neutron scattering moment suggests a large change in the magnetocrystalline anisotropy and band polarization with temperature, although the extremely low effective Debye temperature in the surface region [93] presents a complication to the interpretation of the MCD data that cannot be ignored. Nearest neighbour moment fluctuations [41], resulting in orbital reorientations, would reconcile the spin polarized inverse photoemission and the MCD with the neutron scattering as in the spin polarized inverse photoemission nearest neighbour interactions would only be observed away from the Brillouin zone centre. The proof of temperature dependent orbital hybridization rests on the polarization dependent x-ray absorption spectroscopy described previously.

For the NiMnSb surfaces with a C_{2v} symmetry, the intensity of the s and p polarized absorption signals can be written as [116]:

$$I_S = I_{2,2} + \tfrac{1}{2} I_{2,1} + \tfrac{1}{6} I_{2,0}$$
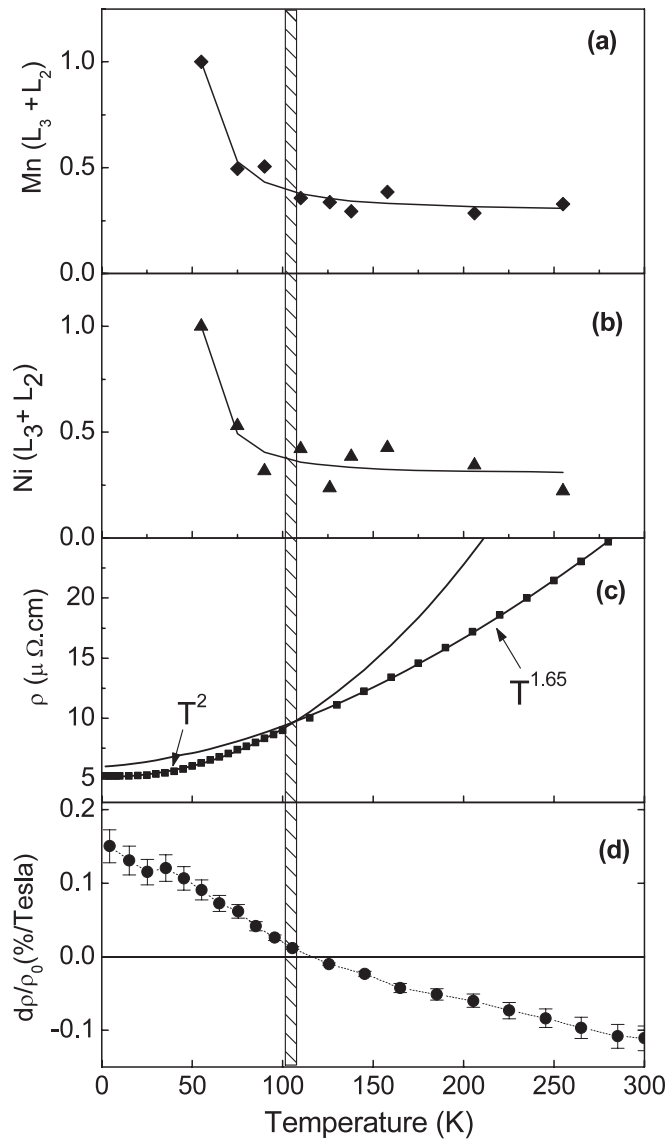$$I_P = I_{2,1} + \tfrac{2}{3} I_{2,0}, \qquad\qquad (21)$$

Figure 33. The (a) Mn and (b) Ni relative magnetic moments derived from MCD from the sum of L_3 and L_2 edges, fitted to an Arrhenius expression and plotted as a function of temperature. (c) The resistance and (d) the longitudinal magnetoresistance slope $(d\rho/\rho_0)$ taken between 2 and 4 T as a function of temperature. Note that the changes in the moment observed in MCD compare well with the onset of changes in the magnetoresistance and resistance in NiMnSb. The T^2 and $T^{1.65}$ curves fitted to the resistance data are as described in the text. Adapted from [33].

where $I_{l,ml}$ is the intensity of the final state transitions of quantum numbers (l, m_l). The corresponding d orbitals are: $d_{x^2-y^2}$ and d_{xy} for $m = 2$, d_{XZ} and d_{YZ} for $m = 1$, and d_{Z^2} for $m = 0$. It is therefore possible to distinguish the contribution of each d orbital in the total absorption signal. Based on this we can conclude on the hybridization of the unoccupied d orbitals in the conduction band, which correspond to the electron states that are accessed in transport measurements.
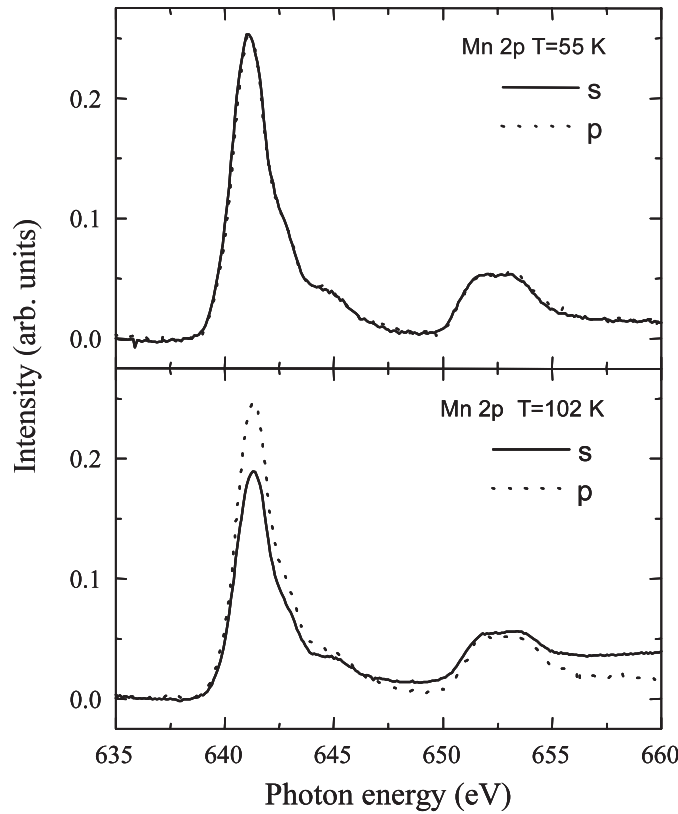
Figure 34. Polarized spectrum $E \parallel z$ (p = dotted line) and $E \perp z$ (s = continuous line) at 55 K (upper panel) and 102 K (lower panel) for the Mn $L_{2,3}$ edges measured by XAS in the total electron yield mode.

Figures 34 and 35 show the absorption spectra at the 2p core levels of the Mn and Ni atoms below (55 K) and above (102 K) the metamagnetic transition temperature at $T = 80$ K, measured in s- and p polarized incident light. We can clearly see a change in the normalized intensities for the two polarizations as a function of temperature. In the case of the Mn atom at 55 K, the s and p polarized spectra are almost the same, while at 102 K the p polarized intensity is enhanced. The reverse is true for the Ni atom—the s polarized spectrum is bigger than p polarized spectrum at 55 K while at 102 K the Ni absorption spectra show almost same intensity.

According to equations (21), we expect an enhanced p polarized spectra compared to the s polarized one when the absorption on the $m_l = \pm 2$ ($I_{2,2}$) states is reduced. When the two linearly polarized spectra are equal, then the $I_{2,2}$ signal must have an important (medium) contribution in order to compensate the $\frac{1}{2}I_{2,1} + \frac{1}{2}I_{2,0}$ signal. Finally, for the case when the s polarized spectrum is more intense than the p polarized one, then the $I_{2,2}$ signal must dominate.

This interpretation can be translated into a reduced $d_{x^2-y^2}$ and d_{xy} orbital contribution to the hybridization between Mn and Ni, as the temperature increases. In fact, in case of the Mn atom at low temperatures, we start from a medium contribution ($I_P = I_S$) of the $I_{2,2}$ signal to the total intensity and we arrive to a low contribution ($I_P > I_S$), at higher temperatures. For the Ni atom, we begin with a strong contribution ($I_P < I_S$) of the $I_{2,2}$ signal to the total intensity at low temperatures and end up with a medium contribution ($I_P = I_S$) at higher temperatures.
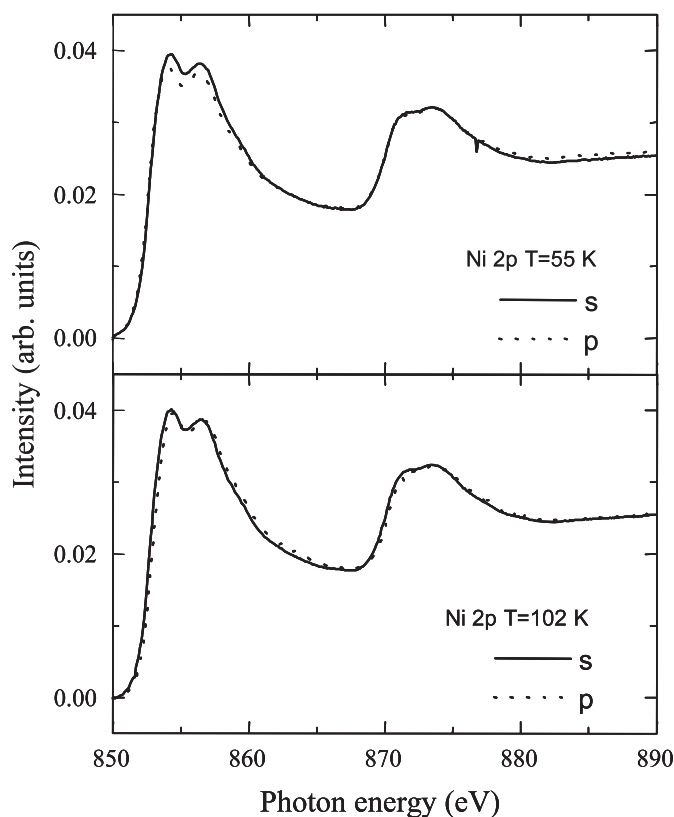
Figure 35. Polarized spectrum $E \parallel z$ (p = dotted line) and $E \perp z$ (s = continuous line) at 55 K (upper panel) and 102 K (lower panel) for the Ni $L_{2,3}$ edges measured by XAS in the total electron yield mode.

Taking into account the geometry of the Mn and Ni sites in the NiMnSb crystal lattice, the best orbital overlap is achieved between the $d_{x^2-y^2}$ and d_{xy} orbitals of Mn and the $d_{XZ,YZ}$ or d_{Z^2} orbital of Ni. On the contrary, the hybridizations between the $d_{XZ,YZ}$ and d_{Z^2} orbitals of the two atoms are not very strong. Since at 55 K the $I_{2,2}$ intensity of Ni is strong, and the one of Mn is medium, while at 102 K the $I_{2,2}$ intensity of Ni is medium and the one of Mn is weak, we must have an enhanced hybridization between the $d_{x^2-y^2}$ with $d_{XZ,YZ}$ or between the d_{xy} with d_{Z^2} orbitals at low temperatures compared to higher temperatures. Therefore, we conclude that the hybridization or the alignment between the Mn and Ni orbital reduces as the temperature increases, as is now suggested from theory [41]. In other words, an orbital reorientation takes place as a function of temperature, switching from a strong hybridization at 55 K to a weak one at 102 K. This reorientation is the result of magnon and phonon effects at finite temperature [36–38, 41] and accounts for the loss of the very high polarization values above 80 K.

8. Is the epitaxial NiMnSb film a true half-metal?

In NiMnSb, the density of states close to the gap is dominated by d states: in the valence band by bonding hybrids with large Ni admixture and, in the conduction band, by the antibonding hybrids with large Mn admixture. Thus the gap originates from the strong hybridization between the d states of the higher valence and the lower valence transition metal atoms. While the Sb atoms (having only s and p states) are not responsible for the existence of the minority

gap, their bands strongly hybridize with the transition metals d states such that the charges in the s, p bands are delocalized. Changing the sp element or changing the orbital hybridization may result in a reduction in polarization [41]. The latter can occur not simply due to defects but also due to spin fluctuations [41] so that the spin minority gap has a maximum value only at $T = 0$ K [36–38, 41]. At finite temperatures, spin disorder increases the spin down density from zero to a non-zero value in the middle of the spin down gap, way above the highest energy level occupied at zero temperature. As a result, the resistance of the spin down channel changes from infinity to a finite value. But even at zero K, the non-quasiparticle density of states [38, 61, 62] should have a small effect and reduce the polarization below 100%.

The multisublattice character of most half-metallic ferromagnets, which is most pronounced in zero-magnetic-field conditions, yields transverse optical phonon modes [36–38] which couple to thermally excited magnons. It may be that longitudinal modes may prove to be even more important [41]. As we can see in figure 25, nearly dispersionless transverse and longitudinal optical modes are observed around 28 meV. Magnon coupling to these phonon modes should result in a dramatic loss in Ni and Mn magnetic moments and therefore, in overall polarization of the NiMnSb. This corresponds to tilting between neighbouring Ni and Mn atoms or to orbital reorientation occurring around 80 K, as shown in section 7. Other models of the temperature dependence of the polarization, due to spin waves have been proposed [41, 44]. It is difficult to envisage how magnons can be eliminated from potential half-metallic systems having more than one sublattice, in order to ensure the true half-metallic character.

At temperatures that are above magnon dominated depolarization, the thermally activated spin mixing mechanism is enhanced by crystal imperfections and by surface and interface effects. Figure 22 showed that a strong chemical potential for surface segregation is present in NiMnSb, indicating that the equilibrium surface has not the same stoichiometry as the bulk thin film [48].

As noted much earlier, the value of 100% spin polarization measured at 300 K at the centre of the Brillouin zone, seen in figure 26, does not provide the evidence of half-metallic behaviour. Polarization at $k_{\parallel} = 0$ corresponds to long range magnetic order but is only loosely related to the magnetic moment. The data shown in figure 30 suggest a very high spin polarization near the Fermi level at 300 K, but as temperature is increased above 80 K, the MCD indicates a decrease in the relative band structure polarization (k integrated). The finite temperature effects, leading to the population of spin minority states near the Fermi level, would be most significant at wavevectors away from $k_{\parallel} = 0$. Similarly, spin minority surface states would also be more evident at wavevectors away from $k_{\parallel} = 0$ [9, 38, 42–46, 105]. Thus neither might be observed by spin polarized inverse photoemission (or spin polarized photoemission) at normal incidence.

Whatever the origin of the depolarization, and the influence of spin waves, half-metallic ferromagnetism should be treated as an idealized limit, realistic only in perfect crystals at zero temperature; if correlation effect are considered, then the non-quasiparticle density of states forbids perfect polarization even in the ground state. Due to finite temperature and surface effects present at the surfaces of NiMnSb films, the classic ferromagnets like Co, Fe or Ni with less than 100% spin polarization may be more reliable for spin injection than the half-metallic systems, especially under ambient or elevated temperatures. It appears that nature abhors half-metallicity [117].

9. Summary

High quality epitaxial NiMnSb thin films have been deposited by facing targets sputtering, using MgO monocrystalline substrates with Mo buffer layers. The epitaxial growth relation

has been found to be (100)NiMnSb ‖ (100)Mo ‖ (110)MgO. Optimum deposition conditions have been determined to achieve highly ordered, continuous films with a low rms roughness. The magnetic and transport properties of the films are comparable to those of bulk single crystals, with the residual resistivity being much lower than what has been reported so far in the literature.

It has been clearly shown by us and others that the surface of NiMnSb(100) is very fragile and surface structure and composition can be easily altered by thermal treatments. The standard sputter and annealing treatments, used to clean most surfaces, lead to Mn segregation or some other surface termination, rarely the stoichiometric surface. For the well-prepared, nearly stoichiometric ordered alloy, the surface appears to terminate in MnSb in agreement with theoretical expectations. Vibrational amplitude of the atoms in the surface and selvedge region were evaluated by extracting the effective Debye temperature using LEED and XPS. Comparing the bulk Debye temperature, obtained by neutron scattering, with the effective Debye temperature of the surface, we find that surface Debye temperature is almost 45% of the bulk value. This drop between the surface and the bulk Debye temperatures can be understood if we take into account that the surface and selvedge regions retain a different composition than the bulk.

The use of different surface preparation methods results in modifications in the surface electronic structure, as theoretically predicted [49, 50, 118]. The general trend is that surface disorder destroys the spin asymmetry near the Fermi level and, therefore, that the assumed half-metals become normal ferromagnets. The maximum spin asymmetry obtained in $k_\parallel = 0$ for a stoichiometric NiMnSb surface was approximately 100% at room temperature. As soon as the Mn segregation is induced by the difference in enthalpy between the surface and the bulk regions, the spin asymmetry at the Fermi level drops to a negative value, which is more reminiscent of MnSb binary alloy or an antiferromagnetically aligned Mn rich surface layer.

The electronic bands closest to the Fermi level are assigned almost entirely to the Mn 3d bands. The valence band of NiMnSb contains a high degree of overlapping between Ni 3d and Mn 3d bands [8, 41, 44]. The first peak in the conduction band of NiMnSb has pure Mn character, which accounts for the high polarization measured at $k_\parallel = 0$.

While it has been suggested that NiMnSb is a half-metallic system [1, 24, 112], it is certainly clear, from the data presented here, that NiMnSb is not a half-metallic ferromagnet above the transition at about 80–100 K, although still well below the ferromagnetic Curie temperature of ∼730 K. Amongst the other potential half-metallic systems, the manganese perovskites have exhibited a number of phase transitions well below the ferromagnetic T_c [94, 97]. The presence of these phase transitions (affecting the moment in the case of NiMnSb) makes clear that finite temperature calculations and measurements that probe the polarization of Fermi level crossings are essential to establish half-metallic ferromagnetism at any appreciable temperature, particularly for the surface. Neither 100% polarization at one k point nor $T^{3/2}$ temperature dependent resistance (sometimes taken as indicative of a half-metallic ferromagnetic [24, 119]) are good indicators of half-metallic behaviour.

40

References

[1] de Groot R A and Mueller F M 1983 *Phys. Rev. Lett.* **50** 2024
[2] de Groot R A, Mueller F M, van Engen P G and Buschow K H J 1984 *J. Appl. Phys.* **55** 2151
[3] Kübler J 1984 *Physica* B **127** 257
[4] Fang C M, de Wijs G A and de Groot R A 2002 *J. Appl. Phys.* **91** 8340
[5] Hanssen K E H M and Mijnarends P E 1986 *Phys. Rev.* B **34** 5009
[6] Galanakis I, Ostanin S, Alouani M, Dreysse H and Wills J M 2000 *Phys. Rev.* B **61** 4093
[7] Kang J-S, Park J-G, Olson C G, Youn S J and Min B I 1995 *J. Phys.: Condens. Matter* **7** 789
[8] Kang J-S, Hong S H, Jung S W, Lee Y P, Park J-G, Olson C G, Youn S J and Min B I 1993 *Solid State Commun.*
     88 635
[9] Galanakis I 2002 *J. Phys.: Condens. Matter* **14** 6329
[10] Galanakis I, Dederichs P H and Papanikolaou N 2002 *Phys. Rev.* B **66** 174429
[11] Galanakis I, Dederichs P H and Papanikolaou N 2002 *Phys. Rev.* B **66** 134428
[12] Liu B G 2003 *Phys. Rev.* B **67** 172411
[13] Xie W H, Xu Y Q, Liu B G and Pettifor D G 2003 *Phys. Rev. Lett.* **91** 037204
[14] Galanakis I 2002 *Phys. Rev.* B **66** 012406
[15] Pickett W E and Singh D J 1996 *Phys. Rev.* B **53** 1146
[16] Singh D J and Pickett W E 1998 *Phys. Rev.* B **57** 88
[17] Kobayashi K-I, Kimura T, Sawada H, Terakura K and Tokura Y 1998 *Nature* **395** 677
[18] Schwarz K 1986 *J. Phys. F: Met. Phys.* **16** L211
[19] van Lueken H and de Groot R A 1995 *Phys. Rev.* B **51** 7176
[20] Korotin M A, Anisimov V I, Khomskii D I and Sawatzky G A 1998 *Phys. Rev. Lett.* **80** 4305
[21] Lewis S P, Allen P B and Sasaki T 1997 *Phys. Rev.* B **55** 10253
[22] de Groot R A and Buschow K H J 1986 *J. Magn. Magn. Mater.* **54–57** 1377
[23] Penicaud M, Silberchoit B, Sommers C B and Kubler J 1992 *J. Magn. Magn. Mater.* **103** 212
[24] Irkhin V Yu and Katsnelson M I 1994 *Phys. Usp.* **37** 659
[25] Mazin I I 2000 *Appl. Phys. Lett.* **77** 3000
[26] Bona L, Meier F, Taborelli M, Bucher E and Schmidt P H 1985 *Solid State Commun.* **56** 391
[27] Soulen R J *et al* 1998 *Science* **282** 85
[28] Miyoshi Y, Bugoslavsky Y, Syed M H, Robinson T, Cohen L F, Singh L J, Barber Z H, Grigorescu C E A,
     Gardelis S, Giapintzakis J and Van Roy W 2006 *Appl. Phys. Lett.* **88** 142512
[29] Sicot M, Turban P, Andrieu S, Tagliaferi A, de Nadai C, Brookes N B, Bertran F and Fortuna F 2006 *J. Magn.*
     Magn. Mater. **303** 54
[30] Wolfgang G 1991 *PhD Thesis* Freie University of Berlin, Germany
[31] Kolev H, Rangelov G, Braun J and Donath M 2005 *Phys. Rev.* B **72** 104415
[32] Ristoiu D, Nozières J P, Borca C N, Komesu T, Jeong H-K and Dowben P A 2000 *Europhys. Lett.* **49** 624
[33] Borca C N, Takashi K, Jeong H-K, Dowben P A, Ristoiu D, Hordequin Ch, Nozières J P, Pierre J, Shane S and
     Idzerda Y U 2001 *Phys. Rev.* B **64** 052409
[34] Ristoiu D 2000 *PhD Thesis* Université Joseph Fourier, Grenoble I, France
[35] Skomski R and Dowben P A 2002 *Europhys. Lett.* **58** 544
[36] Dowben P A and Skomski R 2003 *J. Appl. Phys.* **93** 7948
[37] Dowben P A and Skomski R 2004 *J. Appl. Phys.* **95** 7453
[38] Dowben P A and Jenkins S J 2005 *Frontiers in Magnetic Materials* ed A Narlikar (Berlin: Springer) pp 295–325
[39] Itoh H, Ohsawa T and Inoue J 2000 *Phys. Rev. Lett.* **84** 2501
[40] MacDonald A H, Jungwirth T and Kasner M 1998 *Phys. Rev. Lett.* **81** 705
[41] Lezaic M, Mavropoulos P, Enkovaara J, Bihlmayer G and Blugel S 2006 *Phys. Rev. Lett.* **97** 026404
[42] de Wijs G A and de Groot R A 2001 *Phys. Rev.* B **64** 020402
[43] Jenkins S J and King D A 2001 *Surf. Sci.* **494** L793
[44] Lezaic M, Galanakis I, Bihlmayer G and Blugel S 2005 *J. Phys.: Condens. Matter* **17** 3121
[45] Lezaic M, Mavropoulos P, Bihlmayer G and Blugel S 2006 *J. Phys. D: Appl. Phys.* **39** 797
[46] Galanakis I 2005 *J. Magn. Magn. Mater.* **288** 411
[47] Tanaka C T, Nowak J and Moodera J S 1999 *J. Appl. Phys.* **86** 6239
[48] Ristoiu D, Nozières J P, Borca C N, Borca B and Dowben P A 2000 *Appl. Phys. Lett.* **76** 2349
[49] Orgassa D, Fujiwara H, Schulthess T C and Butler W H 1999 *Phys. Rev.* B **60** 13237
[50] Orgassa D, Fujiwara H, Schulthess T C and Butler W H 2000 *J. Appl. Phys.* **87** 5870
[51] Hordequin C, Pierre J and Currat R 1996 *J. Magn. Magn. Mater.* **162** 75
[52] Hordequin C, Ristoiu D, Ranno L and Pierre J 2000 *Eur. Phys. J.* B **16** 287

[53] Ristoiu D, Nozières J P and Ranno L 2000 *J. Magn. Magn. Mater.* **219** 97
[54] Hordequin C, Nozières J P and Pierre J 1998 *J. Magn. Magn. Mater.* **183** 225
[55] Lewis B and Anderson J C 1978 *Nucleation and Growth of Thin Films* (New York: Academic)
[56] Thornton J A 1982 *Coating Deposition by Sputtering. Deposition Technologies for Films and Coatings*
       (Park Ridge, NJ: Noyes Publications)
[57] Michalowizc A 1990 *Thèse d'état* Univ. Paris Val de Marne
[58] McKale A G 1988 *J. Am. Chem. Soc.* **110** 3763
[59] Hordequin C, Lelievre-Berna E and Pierre J 1997 *Physica* B **234** 602
[60] Skomski R, Zhou J, Dowben P A and Sellmyer D J 2005 *J. Appl. Phys.* **97** 10C305
[61] Chioncel L, Katsnelson M I, de Groot R A and Lichtenstein A I 2003 *Phys. Rev.* B **68** 144425
[62] Irkhin V Y and Katsnelson M I 1985 *J. Phys. C: Solid State Phys.* **18** 4173
[63] Otto M J, van Woerden R A M, van der Valk J P, Wijngaard J, van Bruggen C F and Haas C 1989 *J. Phys.:
       Condens. Matter* **1** 2351
[64] Moodera J S and Mootoo D M 1994 *J. Appl. Phys.* **76** 6101
[65] Dowben P A and Miller A (ed) 1990 *Core-level Spectroscopy and the Characterization of Surface Segregation,
       in Surface Segregation Phenomena* (Boston, MA: CRC Press)
[66] Choi J, Zhang J, Liou S-H, Dowben P A and Plummer E W 1999 *Phys. Rev.* B **59** 13453
[67] Dulli H, Dowben P A, Liou S-H and Plummer E W 2000 *Phys. Rev.* B **62** R14629
[68] Borca C N, Xu B, Komesu T, Jeong H-K, Liu M T, Liou S-H and Dowben P A 2002 *Surf. Sci. Lett.* **512** L346
[69] Seah M P, Jones M E and Anthony M T 1984 *Surf. Interface Anal.* **6** 242
       Seah M P 1993 *Surf. Interface Anal.* **20** 243
[70] Monnier R 1997 *Phil. Mag.* B **75** 67
[71] Foiles S M 1985 *Phys. Rev.* B **32** 7685
[72] Finnis M W and Sinclair J E 1984 *Phil. Mag.* A **50** 45
[73] Bozzolo G, Ferrante J, Noebe R D, Good B, Honecy F S and Abel P 1999 *Comput. Mater. Sci.* **15** 169
[74] Deng H, Hu W, Shu X and Zhang B 2004 *Appl. Surf. Sci.* **221** 408
[75] Jenkins S J 2004 *Phys. Rev.* B **70** 245401
[76] Donath M and Nolting W (ed) 2005 *Local Moment Ferromagnets* (Berlin: Springer) p 245
[77] Tanuma S, Ichimura S and Yoshihara K 1996 *Appl. Surf. Sci.* **101** 47
[78] *NIST Electron Inelastic Mean Free Path Program Version 1.1 (NST std. ref. Database 71)* http://www.nist.gov.
       srd
[79] Jeong H K, Komesu T, Dowben P A, Schultz B D and Palmstrøm C J 2002 *Phys. Lett.* A **302** 217
[80] Briggs D and Seah M P (ed) 1990 *Practical Surface Analysis—Auger and X-ray Photoelectron Spectroscopy*
       vol 1 (Chichester: Wiley)
[81] Scofield J H 1976 *J. Electron Spectrosc. Relat. Phenom.* **8** 129
[82] Penn D R 1976 *J. Electron Spectrosc. Relat. Phenom.* **9** 29
[83] Liu S Y and Kung H H 1981 *Surf. Sci.* **110** 504
[84] Alling B, Shallcross S and Abrikosov I A 2006 *Phys. Rev.* B **73** 064418
[85] Attema J J, Fang C M, Chioncel L, de Wijs G A, Lichtenstein A I and de Groot R A 2004 *J. Phys.: Condens.
       Matter* **16** S5517
[86] Wang S C and Ehrich G 1988 *Surf. Sci.* **206** 457
[87] Roux H, Piquet A, Uzun R and Drechsler M 1976 *Surf. Sci.* **59** 97
[88] Badorf A D and Plummer E W 1990 *J. Electron Spectrosc. Relat. Phenom.* **54/55** 541
[89] Badorf A D and Plummer E W 1991 *Phys. Rev. Lett.* **66** 2770
[90] Benedeck G and Toennies J P 1992 *Phys. Rev.* B **46** 13643
[91] Tung R T, Graham W R and Melmed A J 1982 *Surf. Sci.* **115** 576
[92] King D A and Thomas G 1980 *Surf. Sci.* **91** 201
[93] Borca C N, Ristoiu D, Komesu T, Jeong H K, Hordequin C, Pierre J, Nozières J P and Dowben P A 2000 *Appl.
       Phys. Lett.* **77** 88
[94] Borca C N, Choi J, Adenwalla S, Ducharme S, Dowben P A, Robertson L, Fridkin V M, Palto S P and
       Petukhova N 1999 *Appl. Phys. Lett.* **74** 347
[95] Zhang J and Plummer E W 1997 *Surf. Sci.* **393** 64
[96] Clarke L J 1985 *Surface Crystallography—An Introduction to Low Energy Electron Diffraction* (New York:
       Wiley)
[97] Waldfried C, McIlroy D N, Zhang J, Dowben P A, Katrich G A and Plummer E W 1996 *Surf. Sci.* **363** 296
[98] van Hove M A, Weinberg W H and Chan C-M 1986 *Low-Energy Electron Diffraction* (*Springer Series in
       Surface Science*) vol 6 (Berlin: Springer) p 134

[99] Gopal E S R 1966 *Specific Heats at Low Temperatures* (New York: Plenum) p 29
[100] Kittel C 1996 *Introduction to Solid State Physics* (New York: Wiley) p 90
[101] Hordequin C 1997 *PhD Thesis* Université Joseph Fourier, Grenoble I, France
[102] Yang L and Rahman T S 1991 *Phys. Rev. Lett.* **67** 2327
[103] Ditlevsen P D, Stoltze P O and Nørskov J K 1991 *Phys. Rev.* B **44** 13002
[104] Borca C N, Komesu T and Dowben P A 2002 *J. Electron. Spectrosc. Relat. Phenom.* **122** 259
[105] Correa J S, Eibl C, Rangelov G, Braun J and Donath M 2006 *Phys. Rev.* B **73** 125316
[106] Coehoorn R, Haas C and de Groot R A 1985 *Phys. Rev.* B **31** 1980
[107] Okuda H, Senba S, Sato H, Shimada K, Namatame H and Taniguchi M 1999 *J. Electron. Spectrosc. Relat. Phenom.* **101–103** 657
[108] Panchula A F, Kaiser C, Kellock A and Parkin S S P 2003 *Appl. Phys. Lett.* **83** 1812
[109] Ravidran P, Delin A, James P, Johansson B, Willis J M, Ahuja R and Eriksson O 1999 *Phys. Rev.* B **59** 15680
Rader O *et al* 1998 *Phys. Rev.* B **57** R689
[110] van der Laan G and Kirkman I W 1992 *J. Phys.: Condens. Matter* **4** 4189
[111] de Groot F M F, Hu Z W, Lopez M F, Kaindl G, Guillot F and Tronc M 1994 *J. Chem. Phys.* **101** 6570
[112] Galanakis I, Ostanin S, Alouani M, Dreysse H and Wills J M 2000 *Phys. Rev.* B **61** 4093
[113] Thole B T, Cowan R D, Sawatzky G A, Fink J and Fuggle J C 1985 *Phys. Rev.* B **31** 6856
[114] Stöhr J and König H 1995 *Phys. Rev. Lett.* **75** 3748
[115] Dürr H *et al* 1996 *Phys. Rev. Lett.* **76** 3464
[116] Bianconni A, della Longa S, Li C, Pompa M, Congiu-Castellano A, Udron D, Flank A M and Lagarde P 1991 *Phys. Rev.* B **44** 10126
[117] Paraphrase of remarks by Hathaway K 2005 private communication, Office of Naval Research
[118] Sarma D D 1996 *J. Electron. Spectrosc. Relat. Phenom.* **78** 37
[119] Imada M, Fujimori A and Tokura Y 1998 *Rev. Mod. Phys.* **70** 1039–263